Nanoscale

PAPER

View Article Online
View Journal | View Issue

Cite this: *Nanoscale*, 2026, **18**, 6044

Modeling β-sheet breaker peptides across multiple resolutions: from neurological targets to liposomal membranes

Gulsah Gul

Received 1st December 2025,
Accepted 11th February 2026

DOI: 10.1039/d5nr05060j

rsc.li/nanoscale

β-Sheet-breaker peptides can destabilize protein aggregates associated with neurological disorders, thereby interfering with fibril formation. Given the pivotal role of misfolded protein oligomers such as amyloid-β and α-synuclein in Alzheimer's and Parkinson's diseases, respectively, strategies that block β-sheet formation or perturb β-sheet-rich interactions are promising therapeutic approaches to mitigate neurotoxicity and slow disease progression. However, cross-applicability of inhibitor peptides between these diseases remains largely unexplored. Moreover, the clinical potential of β-sheet-breaker peptides is often limited by enzymatic degradation and restricted blood–brain barrier permeability, necessitating effective delivery systems. To address these challenges, lipid-based nanocarriers offer versatile platforms for peptide encapsulation and controlled release. Therefore, in this study, we collected 50 experimentally validated β-sheet-breaker peptides and examined their binding to amyloid-β and α-synuclein fibrils using molecular docking and molecular dynamics simulations. The selected peptide was further evaluated *via* atomistic and coarse-grained simulations within PEGylated phosphatidylcholine bilayers at varying cholesterol concentrations to assess peptide–lipid interactions and encapsulation potential. Our results indicate that certain peptides may target multiple misfolded proteins, supporting their potential for cross-disease repurposing. Among the candidates, KR peptides exhibited the highest binding free energy toward both targets, while RR peptides demonstrated robust binding with comparable affinity. Multiscale simulations revealed that RR peptides predominantly localize within PEG corona regions and interact with lipid phosphate headgroups, suggesting preferential surface adsorption on pre-formed liposomal fragments. Peptide insertion was more pronounced in unsaturated membranes, whereas cholesterol-rich, saturated membranes hindered permeation and bilayer-to-vesicle transition. Overall, this study provides the first molecular-level insight into the potential of experimentally validated peptides against different neurodegenerative targets and presents a lipid-based delivery strategy to enhance their bioavailability by elucidating the underlying molecular interactions.

Introduction

Alzheimer's and Parkinson's diseases stand as the leading neurodegenerative disorders worldwide, representing a dual challenge that poses a major public health burden and affects millions of lives.[1–3] In both diseases, the accumulation of abnormal protein aggregates (amyloid-β and tau in Alzheimer's, and α-synuclein in Parkinson's) plays a major role in the pathophysiology, causing neuronal dysfunction and cell death.[4] Therefore, despite their distinct clinical manifestations, both disorders share overlapping molecular pathways involving protein misfolding, aggregation, oxidative stress, and impaired proteostasis,[5–7] suggesting that therapeutic strategies developed for one may hold translational potential for the other.

As the conversion of soluble amyloid-β and α-synuclein into β-sheet-rich fibrillar structures drives neuronal dysfunction and disease progression,[8–10] approaches that inhibit β-sheet formation or destabilize early misfolded oligomers have gained considerable interest.[11,12] In this context, β-sheet-breaker peptides designed to disrupt the aggregation of amyloid-β and α-synuclein have emerged as promising therapeutic candidates, with several studies demonstrating their efficacy against Alzheimer's and Parkinson's pathologies. The earliest β-sheet-breaker peptides were developed by substituting proline for valine at residues 17–21 within the central hydrophobic region of Aβ_{1-40}.[13] The resulting pentapeptide LPFFD effectively inhibited amyloid fibrillogenesis and prevented neuronal death *in vitro* by disassembling preformed fibrils.[14] Similarly, the KLVFF peptide, derived from residues

---

Department of Chemical and Biological Engineering, Koç University, İstanbul, Turkey. E-mail: gugul@ku.edu.tr

16–20 of Aβ_{1-40}, was shown to interfere with fibril formation and was suggested to act as an anti-amyloidogenic agent.[15] Subsequent studies expanded this concept, developing β-sheet-breaker peptides of varying motifs and chain lengths targeting amyloid-β or α-synuclein aggregation.[16–19]

While β-sheet-breaker peptides exhibit remarkable efficacy in disrupting fibril formation, they often face limitations such as poor metabolic stability, rapid degradation, and limited blood–brain barrier permeability.[20,21] To address these issues, advanced delivery platforms, particularly lipid-based nanocarriers, have been explored to improve peptide stability, enable controlled release, and central nervous system delivery of therapeutic peptides.[22,23] Indeed, liposomal encapsulation has been shown to enhance peptide stability and circulation time; for instance, the antitumor endostatin peptide exhibited increased plasma half-life and stability when delivered *via* liposomes.[24] Moreover, brain-targeted liposomal formulations have demonstrated significant promise in neurodegenerative disease models by increasing blood–brain barrier permeability and reducing pathological protein aggregation, as shown in a recent study utilizing monoclonal antibody-loaded liposomes for Parkinson's therapy.[25] Along similar lines, CeO_2-loaded liposomal nanoparticles modified with the KLVFF peptide have shown potent anti-amyloidogenic and antioxidative activities, effectively inhibiting Aβ aggregation while scavenging reactive oxygen species.[26] To date, however, only one study has reported the liposomal delivery of β-sheet-breaker peptides, in which the H102 peptide achieved effective brain targeting and significantly improved spatial memory impairment in rats through nasal delivery.[27]

Despite growing interest in the use of peptides as therapeutic agents or targeting moieties for neurological diseases, the molecular mechanisms underlying their interactions with target proteins remain poorly understood. In this context, molecular modeling approaches offer valuable tools not only for the rational design of new inhibitors but also for elucidating peptide binding mechanisms, stability, energetics, and encapsulation behavior within lipid environments.[28–30] So far, there has been no systematic or comparative evaluation of available peptide inhibitors across different targets, including their dual-targeting capabilities. Although several studies have aimed to design novel peptide inhibitors *via* molecular docking calculations,[30–32] none have integrated multiple existing and structurally diverse peptides to comparatively assess their inhibitory potential against amyloidogenic targets. Moreover, interactions between β-sheet-breaker peptides and lipid-based nanocarriers, either in planar bilayers or vesicular architectures, have not yet been explored through molecular dynamics simulations.

In this context, this work represents a pioneering effort in peptide repurposing between Alzheimer's and Parkinson's diseases and proposes a systematic targeted design strategy for peptide-loaded liposomes in neurological applications, highlighting the potential of β-sheet breaker peptides as delivery candidates within a comparative framework encompassing both planar lipid membranes and liposomal assemblies.

Computational methods

Peptide discovery *via* molecular docking

Short-chain peptides that were experimentally shown to have beta-sheet-breaking activity against toxic amyloid-β and α-synuclein fibrils, which contribute to the progression of neurodegenerative diseases, were screened in the literature and are summarized in Table 1. Accordingly, 52 beta-sheet-breaking peptide sequences ranging from five to 12 monomers in length were identified. Peptides with cyclic structures, ambiguous residues, chemical modifications, or those designed solely as targeting moieties or without experimental validation were excluded to maintain dataset consistency. For subsequent analyses, LVFFA was omitted because of its weak binding capacity, reflected by ~92% fibril retention[13] while Ac-LVFFARK-NH_2 was excluded because of its reported cytotoxicity.[33]

To assess the inhibitory potential of 50 peptides in the final dataset, molecular docking calculations were performed against amyloid-β (Aβ) and α-synuclein (αSyn) fibril structures. The peptide sequences were generated in linear form using the *PeptideBuilder.py script*.[54] To increase the stability of the peptides, an acetyl (Ac) group was added to the N-terminus, and an amide (NH_2) group was added to the C-terminus. The protein crystal structures of the fibrillar form of Aβ (PDB ID: 2MXU) and αSyn (PDB ID: 2N0A) was downloaded from the Protein Data Bank, and protonation states were assigned at pH 7.4 using the Propka3[55] server. Then, potential binding pockets were scanned with Schrödinger's SiteMap[56] module, and the corresponding active site residues are listed in Table 2 with their drug-likeness scores (D-scores). It should be noted that αSyn fibril has multiple binding sites (~13 putative sites reported) and, in this study, site2 as defined by Hsieh *et al.* comprising Y39, S42, T44 residues was selected for primary docking[57] because of its more favorable scoring energies reported for small molecule inhibitors.[58] In addition, site 3/13 (K43, K45, V48, and H50), also reported by Hsieh *et al.* (2018),[57] was illustrated because some peptides showed a preference for this region within the defined grid box. In contrast, the amyloid-β (Aβ) fibril structure (PDB ID: 2MXU) was found to possess a single active site, including residues H14, L17, I32, and G33 across all chains, consistent with previous reports,[59] and referred to here as site1. These active sites are depicted in Fig. 1 and further confirmed by blind docking with the peptide sequences in Table 1.

Protein–peptide docking calculations were performed using AutoDock CrankPep (ADCP),[60] a software previously developed and validated for protein–protein docking analyses. The grid box was centered at coordinates $x = -3.155$ Å, $y = 2.971$ Å, $z = -6.414$ Å for 2MXU and $x = 93.540$ Å, $y = 147.252$ Å, $z = -3.988$ Å for 2N0A, based on the geometric centers of the identified active site residues. Grid box sizes were set to $34 \times 30 \times 30$ Å^3 for 2MXU and $34 \times 45 \times 34$ Å^3 for 2N0A to accommodate peptides of varying lengths. Each docking simulation was repeated three times to rank peptide binding performance, and the average binding energy scores were evaluated for comparative interpretation. To further validate the results, docking

Table 1 List of short-chain (≤12) beta-sheet-breaker peptides extracted from the literature, arranged in chronological order

No.	Peptide name	Peptide sequence	Amino acid length	Template	Target protein	Type	Terminal group	Ref.
1		KLVFF	5	Aβ(16–20)	Aβ(1–40)	L-Enantiomer	None and Ac–	15
2		QKLVFF	6	Aβ(16–20)	Aβ(1–40)	L-Enantiomer	Ac–…–NH$_2$	15
3	AβTT	QKLVTTAE	8	Aβ(17–24) FF_to_TT_substitute	Aβ(1–40)	L-Enantiomer	None	34
4		LVFFA	5	Aβ(17–21)	Aβ(1–40) Aβ(1–42)	L-Enantiomer	None	13
5	iAβ11	RDLPFFPVPID	11	Aβ(17–21)	Aβ(1–40) Aβ(1–42)	L-Enantiomer L- and D-enantiomer	None	13 and 35
6	iAβ5	LPFFD	5	Aβ(17–21)	Aβ(1–40) Aβ(1–42)	L-Enantiomer	Ac–…–NH$_2$	13 and 14
7	YiAβ11	RDLPFYPVPID	11	Aβ(17–21)	Aβ(1–40) Aβ(1–42)	L- and D-enantiomer	None	35
8		GVVIA	5	Aβ(38–42)	Aβ(1–42)	L-Enantiomer	–NH$_2$	28
9		KLVFFA	6	Aβ(16–20)	Aβ(1–40) Aβ(1–42)	L- and D-enantiomer	–NH$_2$	36
10		KKLVFFA	7	Aβ(16–20)	Aβ(1–40) Aβ(1–42)	L- and D-enantiomer	None	36
11		KFVFFA	6	Aβ(16–20)	Aβ(1–40) Aβ(1–42)	L- and D-enantiomer	–NH$_2$	36
12		KIVFFA	6	Aβ(16–20)	Aβ(1–40) Aβ(1–42)	D-Enantiomer	–NH$_2$	36
13		KVVFFA	6	Aβ(16–20)	Aβ(1–40) Aβ(1–42)	D-Enantiomer	–NH$_2$	36
14	ASI1	RGGAVVTGR	9	αSyn(68–72)	αSyn	L-Enantiomer	–NH$_2$	37
15	ASI2	GGAVVTGR	8	αSyn(68–72)	αSyn	L-Enantiomer	–NH$_2$	37
16	ASI3	RGAVVTGR	8	αSyn(68–72)	αSyn	L-Enantiomer	–NH$_2$	37
17		LPYFD	5	Aβ(17–21)	Aβ(1–42)	L-Enantiomer	–NH$_2$	38
18	OR1 and OR2	RGKLVFFGR	9	Aβ(16–20)	Aβ(1–40) Aβ(1–42)	L-Enantiomer	None and –NH$_2$	39
19	Dpep	QSHYRHISPAQV	12		Aβ(1–42)	D-Enantiomer	None	40
20	D3	RPRTRLHTHRNR	12		Aβ(1–42)	D-Enantiomer	None	41
21	V66S-11mer	QVTNSGGAVVT	11	αSyn(62–72)	αSyn	L-Enantiomer	–NH$_2$	42
22	V66P-8mer	VTNPGGAV	8	αSyn(63–70)	αSyn	L-Enantiomer	–NH$_2$	42
23	T72P-10mer	GAVVPGVTAV	10	αSyn(68–77)	αSyn	L-Enantiomer	Ac–…–NH$_2$	42
24	V74E-11mer	AVVTGETAVAQ	11	αSyn(69–79)	αSyn	L-Enantiomer	Ac–…–NH$_2$	42
25	V74G-11mer	AVVTGGTAVAQ	11	αSyn(69–79)	αSyn	L-Enantiomer	Ac–…–NH$_2$	42
26	T75P-12mer	VTGVPAVAQK	10	αSyn(71–80)	αSyn	L-Enantiomer	Ac–	42
27	V48P-11mer	KEGPVHGVATV	11	αSyn(45–55)	αSyn	L-Enantiomer	–NH$_2$	42
28	G67P-9mer	VTNVPGAVV	9	αSyn(63–71)	αSyn	L-Enantiomer	–NH$_2$	42
29	T72 K-10mer	GAVVKGVTAV	10	αSyn(68–77)	αSyn	L-Enantiomer	Ac–…–NH$_2$	42
30	T72P-9mer	AVVPGVTAV	9	αSyn(69–77)	αSyn	L-Enantiomer	Ac–…–NH$_2$	42
31	T72P-8mer	VVPGVTAV	8	αSyn(70–77)	αSyn	L-Enantiomer	Ac–…–NH$_2$	42
32	T72P-7mer	VPGVTAV	7	αSyn(71–77)	αSyn	L-Enantiomer	–NH$_2$	42
33	T72P-6mer	PGVTAV	6	αSyn(72–77)	αSyn	L-Enantiomer	–NH$_2$	42
34	T72P-8mer′	AVVPGVTA	8	αSyn(69–76)	αSyn	L-Enantiomer	Ac–…–NH$_2$	42
35	T72P-7mer′	AVVPGVT	7	αSyn(69–75)	αSyn	L-Enantiomer	Ac–…–NH$_2$	42
36	V66S-8mer	VTNSGGAV	8	αSyn(63–70)	αSyn	L-Enantiomer	–NH$_2$	42
37	β-syn36 and β-syn36D	GVLYVGSKTR	10	βSyn36–45	αSyn	L- and D-enantiomer	None	43
38	Retro inverso β-syn 36	RTKSGVYLVG	10	βSyn36–45	αSyn	D-Enantiomer	None and Ac–…–NH$_2$	43
39		PGKLVYA	7	Aβ(16–20)	Aβ(1–42)	L-Enantiomer	None	44
40	KR[a]	KKLVFFARRRRA	12	Aβ(16–20)	Aβ(1–42)	L-Enantiomer	None	44
41	RR	RYYAAFFARR	10	Aβ(11–23)	Aβ(1–40)	L-Enantiomer	Ac–…–NH$_2$	45
42		LPFFN	5	Aβ(17–21)	Aβ(1–40)	L-Enantiomer	Ac–…–NH$_2$	46
43	H102	HKQLPFFEED	10	Aβ(17–21)	Aβ(1–42)	L-Enantiomer	None	47
44	45–54W	KDGIVNGVKA	10	αSyn(45–54)	αSyn	L-Enantiomer	None	16
45	LK7	LVFFARK	7	Aβ(17–21)	Aβ(1–42)	L-Enantiomer	Ac–…–NH$_2$	33
46		IGLMVG	6	Aβ(32–37)	Aβ(1–42)	L-Enantiomer	–NH$_2$	48
47	DB3	RPITRLRTHQNR	12		Aβ(1–42)	D-Enantiomer	–NH$_2$	49
48		KISVRV	6	αSyn(70–75)	αSyn	L-Enantiomer	None	50
49		GQTYVLPG	8	αSyn(46–53)	αSyn	L-Enantiomer	None	50
50	HPYD	HKQLPFYEED	10	Aβ(17–21) FF_to_FY substitution	Aβ(1–42)	L-Enantiomer	None	51
51	46–54W	DGIVAGVKA	9	αSyn(46–54)	αSyn	L-Enantiomer	Ac–…–NH$_2$	52
52	PDpep1.3[b]	DEEIERQLKALG	12		αSyn	L-Enantiomer	None	53

[a] Peptide name is given in this study because of convenience. [b] Peptide name is abbreviated as Pep1.3 for the rest of this article.

Table 2 Active site residues of the amyloid-β (PDB ID: 2MXU) (D-score = 1.29) and α-synuclein fibril (PDB ID: 2N0A) (D-score = 1.09)

2MXU protein chain ID	Active site residue no.	2N0A protein chain ID	Active site residue no.
A	V12, H14, L17, I32, G33, L34	A	Y39, S42, T44
B	V12, H14, L17, I32, G33, L34	B	Y39, S42, T44
C	V12, H14, L17, I32, G33, L34	C	Y39, S42, K43, T44
D	V12, H14, L17, I32, G33, L34	D	Y39, S42, K43, T44
E	V12, H14, L17, I32, G33, L34	E	Y39, S42, K43, T44
F	V12, H14, L17, I32, G33, L34	F	Y39, S42, K43, T44
G	H14, L17, I32, G33	G	Y39, S42, K43, T44
H	H14, L17, I32, G33, L34	H	Y39, S42, K43, T44
I	L17, I32, G33, L34	I	Y39, S42, K43, T44
J	H14, L17, I32, G33, L34	J	Y39, S42, T44
K	H14, Q15, L16, V17, I32, G33, L34		
L	H14, L16, V17, I32, G33		

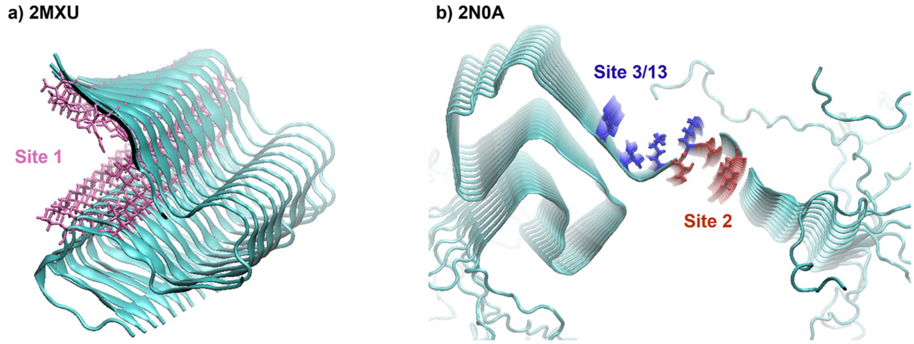

Fig. 1 Binding sites of amyloid-β (PDB ID: 2MXU) and α-synuclein (PDB ID: 2N0A) fibrils. Here, K43 is shared among some chains between site 2 and site 3/13 of 2N0A, however, it's visualized as part of site 3/13 to maintain consistency with the literature.

calculations were also conducted with the HPEPDOCK,[61] another software designed for protein–protein docking that supports both site-specific and blind docking modes.

Peptide stability *via* molecular dynamics

The binding stability of Pep1.3, H102 and HPYD peptides, based on the ADCP average binding scores data listed in Table 3, and the RR and KR sequences, based on the HPEPDOCK binding energy data, were investigated for their binding stability through 2MXU and 2N0A using MD simulations. For this purpose, the protein–peptide complexes obtained by docking were placed in a cubic box with an edge length of 10.5 nm and 19.8 nm for 2MXU and 2N0A systems, respectively. The systems were solvated with the TIP3P water model and 0.15 M NaCl salt using the CHARMM-GUI software.[62,63] All simulations were performed with GROMACS 2021.3[64] software with the CHARMM36m[65] force field. First, the energy of the systems was minimized using the steepest descent algorithm, and the resulting structures were equilibrated for 5 ns with a position restraint on peptides under constant particle number, volume, and temperature (NVT) conditions. The cutoff distance for van der Waals and electrostatic interactions was set to 1.2 nm and van der Waals interactions were switched off between 1.0 and 1.2 nm using the force-switch modifier. Long-range electrostatic interactions were calculated using the particle mesh Ewald (PME) method,[66] and the hydrogen bonds were constrained with the LINCS algorithm.[67] The temperature was maintained at 310 K using a V-rescale thermostat[68] with a time constant of 1.0 ps. Molecular Dynamics (MD) simulations were run under constant particle number, pressure, and temperature (NPT) ensemble for 100 ns with a time step of 2 fs. The pressure of the systems was controlled isotropically by the Parrinello–Rahman barostat[69] with a coupling constant of 5 ps at 1 bar and a compressibility factor of 4.5×10^{-5} bar^{-1}.

Root-mean-square deviation (RMSD) analyses were performed using *gmx rms* to determine the structural stability of the peptides along the simulation trajectories. The fibril backbones were first aligned to the reference minimized structures, and then RMSD of the peptide backbones was calculated relative to the aligned fibrils. The binding free energies to the target molecule were calculated using the *gmx_mmpbsa* module over the last 25 ns of the trajectory, with a total of 250 frames analyzed for each replica. Then binding free energy of the protein–peptide complexes was determined as described in eqn (1):

$$\Delta G_{\text{binding}} = \langle G_{\text{complex}} \rangle - (\langle G_{\text{protein}} \rangle + \langle G_{\text{peptide}} \rangle) \qquad (1)$$

where G represents the average total free energy, consisting of both gas-phase and solvation free energy contributions.[70]

Table 3 Binding scores of β-sheet breaker peptides on amyloid-β (2MXU) and α-synuclein (2N0A) fibrils, calculated by ADCP and HPEPDOCK molecular docking tools. Peptide sequences are listed with respect to their average ADCP binding scores in descending order

	2MXU						2N0A				
Peptide sequence	ADCP-Trial1	ADCP-Trial2	ADCP-Trial3	ADCP-Avg	HPEPDOCK	Peptide sequence	ADCP-Trial1	ADCP-Trial2	ADCP-Trial3	ADCP-Avg	HPEPDOCK
DEEIERQLKALG	−20.9	−19.4	−19.9	−20.1	−165.3	KKLVFFARRRRA	−23.4	−22.4	−23.3	−23.0	−292.6
HKQLPFFEED	−18.8	−19.7	−19.8	−19.4	−226.5	DEEIERQLKALG	−20.8	−23.9	−23.0	−22.6	−185.1
KKLVFFARRRRA	−19.0	−19.9	−18.7	−19.2	−257.4	HKQLPFFEED	−22.1	−22.7	−22.1	−22.3	−186.1
HKQLPFYEED	−18.5	−18.4	−18.5	−18.5	−223.1	RPRTRLHTHRNR	−23.5	−21.3	−21.3	−22.0	−254.2
RYYAAFFARR	−17.8	−18.2	−17.4	−17.8	−296.0	HKQLPFYEED	−20.0	−20.7	−21.9	−20.9	−195.3
RTKSGVYLVG	−16.6	−17.5	−16.8	−17.0	−235.9	RPITRLRTHQNR	−20.1	−21.1	−18.6	−19.9	−277.3
RGKLVFFGR	−16.4	−17.5	−17.0	−17.0	−228.3	RYYAAFFARR	−18.9	−18.9	−20.0	−19.3	−278.8
QSHYRHISPAQV	−16.4	−16.5	−17.4	−16.8	−276.2	RGKLVFFGR	−17.4	−18.2	−19.2	−18.3	−247.4
GVLYVGSKTR	−14.9	−17.9	−16.3	−16.4	−234.1	GVLYVGSKTR	−16.7	−18.8	−16.8	−17.4	−213.6
RPITRLRTHQNR	−16.0	−16.4	−16.0	−16.1	−237.7	KDGIVNGVKA	−17.6	−17.3	−16.8	−17.2	−160.1
RPRTRLHTHRNR	−15.1	−15.9	−17.2	−16.1	−245.1	RTKSGVYLVG	−17.3	−18.0	−15.9	−17.1	−207.0
QVTNSGGAVVT	−15.9	−15.5	−16.1	−15.8	−210.3	KKLVFFA	−16.6	−16.2	−17.1	−16.6	−211.8
RDLPFFPVPID	−15.5	−14.3	−17.6	−15.8	−240.7	KEGPVHGVATV	−17.9	−16.2	−15.6	−16.6	−183.8
KDGIVNGVKA	−15.5	−15.7	−16.2	−15.8	−163.8	QSHYRHISPAQV	−14.8	−17.1	−17.2	−16.4	−282.3
KKLVFFA	−15.4	−15.8	−16.1	−15.8	−221.0	QKLVTTAE	−15.7	−16.2	−16.9	−16.3	−154.7
AVVTGGTAVAQ	−15.9	−15.7	−15.5	−15.7	−230.2	QKLVFF	−15.9	−15.7	−15.6	−15.7	−190.8
VTGVPAVAQK	−15.5	−15.2	−15.7	−15.5	−225.4	RDLPFFPVPID	−14.6	−16.3	−16.0	−15.6	−217.7
KEGPVHGVATV	−14.4	−14.8	−17.0	−15.4	−223.2	KISVRV	−14.8	−15.1	−14.9	−14.9	−169.0
AVVTGETAVAQ	−15.3	−15.3	−14.0	−14.9	−222.4	RGGAVVTGR	−13.7	−16.6	−14.2	−14.8	−188.3
QKLVTTAE	−15.0	−14.4	−14.9	−14.8	−158.3	GAVVKGVTAV	−14.8	−14.1	−15.3	−14.7	−162.0
KIVFFA	−14.4	−14.4	−14.9	−14.6	−190.7	AVVTGETAVAQ	−14.6	−14.7	−14.7	−14.7	−182.8
QKLVFF	−14.8	−14.0	−14.8	−14.5	−196.4	KIVFFA	−14.6	−15.0	−14.3	−14.6	−198.5
DGIVAGVKA	−14.2	−14.8	−14.5	−14.5	−172.2	RGAVVTGR	−15.1	−13.9	−14.9	−14.6	−186.9
KFVFFA	−14.3	−14.5	−14.2	−14.3	−209.3	KFVFFA	−14.1	−15.2	−14.5	−14.6	−215.7
PGKLVYA	−14.9	−13.8	−14.2	−14.3	−194.8	DGIVAGVKA	−13.8	−14.8	−15.1	−14.6	−153.6
GAVVKGVTAV	−14.5	−14.1	−14.1	−14.2	−225.3	PGKLVYA	−14.5	−14.2	−14.9	−14.5	−208.3
RDLPFYPVPID	−15.9	−12.8	−13.9	−14.2	−247.0	RDLPFYPVPID	−12.9	−16.0	−14.7	−14.5	−205.0
RGGAVVTGR	−14.7	−13.7	−13.8	−14.1	−204.7	LPYFD	−14.4	−14.6	−14.4	−14.5	−158.4
KLVFFA	−14.4	−13.5	−14.0	−14.0	−195.0	KLVFFA	−14.6	−14.3	−14.4	−14.4	−199.8
KVVFFA	−13.2	−13.5	−13.8	−13.5	−182.2	AVVTGGTAVAQ	−14.2	−14.1	−14.8	−14.4	−178.1
VTNVPGAVV	−13.4	−13.7	−13.3	−13.5	−219.2	QVTNSGGAVVT	−14.8	−14.5	−13.5	−14.3	−189.7
LPYFD	−14.0	−12.7	−13.4	−13.4	−179.3	LPFFD	−13.6	−14.1	−14.6	−14.1	−179.3
KISVRV	−13.6	−13.3	−13.1	−13.3	−167.6	VTGVPAVAQK	−14.1	−14.4	−13.7	−14.1	−190.6
VTNSGGAV	−14.6	−12.7	−12.7	−13.3	−166.0	KVVFFA	−14.7	−13.4	−14.0	−14.0	−191.1
KLVFF	−13.3	−13.2	−13.4	−13.3	−177.0	KLVFF	−13.8	−14.2	−13.9	−14.0	−195.3
RGAVVTGR	−13.2	−13.2	−13.4	−13.3	−173.8	GQTYVLPG	−12.7	−14.0	−12.9	−13.2	−189.4
LPFFD	−13.4	−13.0	−13.3	−13.2	−163.4	LPFFN	−13.1	−12.8	−12.0	−12.6	−194.2
GAVVPGVTAV	−13.2	−13.4	−13.0	−13.2	−215.4	AVVPGVTAV	−13.2	−12.4	−12.2	−12.6	−161.9
GQTYVLPG	−12.8	−13.4	−12.6	−12.9	−209.0	GGAVVTGR	−12.2	−13.0	−12.3	−12.5	−165.9
AVVPGVTAV	−12.7	−13.3	−12.3	−12.8	−205.8	VTNSGGAV	−12.4	−13.3	−11.8	−12.5	−138.8
LPFFN	−13.0	−12.1	−12.8	−12.6	−179.7	VTNVPGAVV	−11.6	−12.5	−12.7	−12.3	−158.8
VTNPGGAV	−12.3	−12.9	−12.0	−12.4	−177.0	VVPGVTAV	−12.6	−12.6	−11.0	−12.1	−159.5
VVPGVTAV	−12.8	−12.6	−11.7	−12.4	−192.7	IGLMVG	−12.1	−12.0	−11.7	−11.9	−149.4
AVVPGVTA	−13.6	−11.8	−11.5	−12.3	−184.5	GAVVPGVTAV	−12.8	−11.3	−11.4	−11.8	−182.1
IGLMVG	−12.0	−12.4	−12.1	−12.2	−164.1	PGVTAV	−11.0	−11.6	−10.8	−11.1	−145.0
GGAVVTGR	−11.6	−11.9	−12.7	−12.1	−188.5	VTNPGGAV	−11.1	−11.5	−10.6	−11.1	−144.4
AVVPGVT	−11.5	−12.5	−12.1	−12.0	−172.2	AVVPGVTA	−11.4	−10.2	−11.0	−10.9	−147.5
VPGVTAV	−11.3	−11.5	−11.3	−11.4	−176.9	VPGVTAV	−10.6	−11.2	−10.6	−10.8	−146.4
PGVTAV	−10.5	−11.2	−11.1	−10.9	−157.7	GVVIA	−10.3	−10.5	−9.6	−10.1	−111.2
GVVIA	−10.5	−10.2	−9.9	−10.2	−132.4	AVVPGVT	−10.0	−10.0	−9.4	−9.8	−141.4

It should be noted that the 2N0A complex systems were computationally demanding, and both the MD simulations and MM/PBSA calculations imposed a considerable computational cost. Therefore, instead of performing a single long simulation for each system, three independent replicas of 100 ns were conducted to ensure reproducibility. The results were further validated by analyzing the interface area between the peptide and the target protein, as calculated using eqn (2):

$$\text{Interface Area} = \text{SASA}_{\text{protein}} + \text{SASA}_{\text{peptide}} - \text{SASA}_{\text{complex}} \quad (2)$$

where SASA denotes the solvent-accessible surface area obtained through the *gmx sasa* module of GROMACS.

In the trajectories where the peptides are stable, protein–peptide interactions (hydrogen bonds, electrostatic interactions, hydrophobic interactions *etc.*) were analyzed and visualized with the VMD[71] program and LigPlot+ (ref. 72) software. Hydrogen bonds were identified employing a donor–acceptor distance cutoff of 0.35 nm and an angle cutoff of 30°, which are widely accepted thresholds for defining hydrogen bonds in MD simulations.

Atomistic peptide–lipid bilayer simulations

A representative configuration of the RR peptide, identified as the most stable conformation based on peptide stability analyses, was obtained by cluster analysis of equilibrated trajectories. This configuration was subsequently positioned in atomistic lipid membrane systems at a 1 : 100 peptide-to-lipid ratio (corresponding to three peptide molecules), approximately 1–1.5 nm above the bilayer surface, using VMD[71] software. To investigate the influence of lipid saturation on peptide translocation, DMPC and DOPC lipids were selected as model liposomal systems. To mimic optimal blood circulation in realistic nanocarriers, 5% PEGylated PC lipids were incorporated. Additionally, the structural stability of the liposomes was examined at low (5%) and high (35%) cholesterol (CHOL) levels.

Prior to production runs, positional restraints were applied to the peptides to prevent atomic clashes and allow the systems to equilibrate. The restraints were then released, and MD simulations were performed for 400 ns for each system in duplicates. System convergence was assessed based on the stability of total energy and key bilayer structural properties. Pressure was maintained at 1 bar using a semi-isotropic Parrinello–Rahman barostat[69] with a coupling constant of 5 ps and a compressibility of 4.5×10^{-5} bar^{-1}. Other simulation parameters were identical to those described in the Peptide stability *via* molecular dynamics section.

Trajectory analyses were conducted over the final 100 ns of each simulation. The area per molecule (APM) was estimated by dividing the box area in the *xy* plane by the number of molecules in a single leaflet. For area-per-lipid (APL) calculations, the molecular area of each cholesterol (CHOL) was taken as 0.39 nm^2, consistent with previous reports,[73,74] and the total cholesterol area was subtracted from the box area before dividing by the number of lipids in one leaflet. Bilayer thickness was calculated from the center-of-mass (COM) distance between the phosphorus (P) atoms of the outer and inner leaflets. Diffusion constants were derived from the mean-square displacement (MSD) functions of phosphorus atoms obtained through the *gmx msd* module, while the density profiles of system components were calculated relative to the membrane center using *gmx density*. The lipid order parameters were determined according to eqn (3):

$$S_{\text{CD}} = \frac{1}{2}\left(3\left\langle\cos^2\theta\right\rangle - 1\right) \quad (3)$$

where θ represents the angle between the bilayer normal and the vector along a specific bond within the lipid tail. An S_{CD} value of 0 corresponds to a completely random orientation, whereas 1 indicates perfect alignment with the bilayer normal. It should be noted that *gmx order* may produce inaccuracies for unsaturated C–H bonds;[75] however, in this study, the focus was on the relative trends in lipid ordering rather than on the exact absolute values.

Coarse-grained peptide–lipid self-assembly simulations

Coarse-grained molecular dynamics (MD) simulations were performed using the Martini 3 force field,[76] which has been validated for lipid system simulations, with GPU acceleration in GROMACS 2021.3. Since the Martini3 coarse-grained model of DMPC is not available, DLPC lipids (5% PEGylated with DLPE_PEG), which closely resemble DMPC, were employed. As we didn't observe significant changes between 0 and 5% CHOL at atomistic simulations, the effect of CHOL was examined at concentrations of 0%, 15%, and 35%. The total lipid number was preserved as 3549 and lipid-to-water molar ratio was set to 1 : 95 in all systems.

For the self-assembly simulations, all lipid molecules, water, and salt ions (0.15 M) were randomly distributed within a cubic simulation box with an edge length of 40 nm. PEGylated DLPC lipids were constructed using the *polyply.py* script[77] with PEG chains of 2000 Da terminated with hydroxyl (OH) groups. Energy minimization was performed using the steepest descent algorithm, followed by equilibration in the NPT ensemble with 10 fs and 20 fs time steps, each for 100 ns. During equilibration, isotropic pressure coupling was applied using the Berendsen barostat[78] with a coupling constant of 5 ps to maintain the pressure at 1 bar. The temperature was kept constant at 310 K using a velocity-rescale thermostat[68] with a coupling time of 1.0 ps. Non-bonded interactions were truncated at 1.1 nm. Lennard-Jones interactions were shifted using the Potential-Shift-Verlet scheme, while electrostatic interactions were treated using the Reaction Field method[79] with a relative dielectric constant (ε_{r}) of 15. Production MD simulations were conducted for 10 μs with a 20 fs time step in duplicates. The system pressure was maintained at 1 bar using an isotropic Parrinello–Rahman barostat[69] with a coupling constant of 12 ps and a compressibility of 4.5×10^{-5} bar^{-1}. In consistent with experiments,[80,81] peptide molecules were introduced into the pre-equilibrated systems (after 100 ns) with 1 : 40 peptide-to-lipid mass ratio at random positions, and the

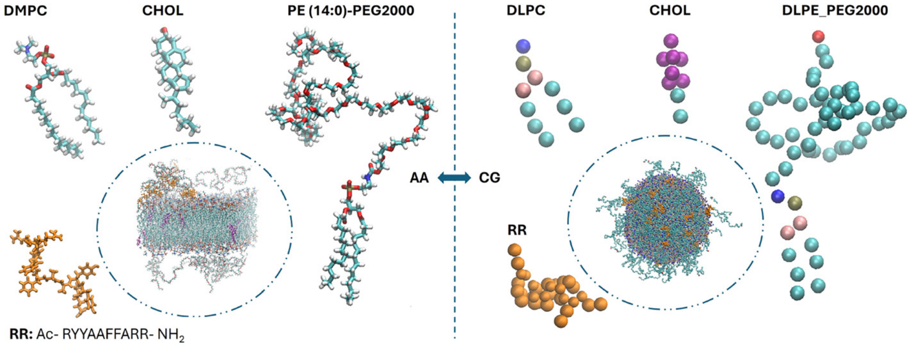

Fig. 2 Overview of the multi-resolution simulation strategy used for comparative analysis of membrane systems. Atomistic (AA) representations of membrane components and the RR peptide, simulated using the CHARMM36m force field, are shown on the left, while coarse-grained (CG) representations based on the MARTINI 3 model are shown on the right. Rather than deriving CG parameters from AA simulations, established force fields are employed independently at each resolution. The central panels illustrate representative self-assembled membrane systems at AA and CG resolutions, highlighting membrane organization.

same equilibration and production protocols were applied. The multiscale linkage between atomistic and coarse-grained simulations, used for comparative analysis, is illustrated in Fig. 2.

Due to the complexity of the systems, simulations did not converge to a single well-defined membrane or vesicle morphology, and multiple irregular lipid assemblies were observed throughout the trajectories. Therefore, convergence was not assessed based on global membrane morphology but rather on the temporal stability of local interaction metrics. Total energy, peptide–lipid contact patterns, pairwise interaction energies and peptide proximity to lipid headgroups exhibited stable distributions without systematic drift during the final 1 µs of the simulations, which was used for subsequent analyses. The radial distribution of peptides relative to phosphate (PO_4) beads were determined *via gmx rdf* while number of contacts for each lipid type (DLPC, DLPE and CHOL) was measured at 0.6 nm distance as a function of time and normalized to 1 by dividing the number of corresponding lipid type. The non-bonded interaction energies were analyzed *via gmx energy* module.

Results & discussion

Molecular docking calculations for peptide discovery

Several peptide-based inhibitors have been developed to interfere with the aggregation of amyloidogenic proteins, or to promote the disassembly of existing fibrils, which are key pathological features of many neurodegenerative diseases. These inhibitors may act by binding monomeric or oligomeric species to prevent β-sheet formation,[44,45] and/or by directly interacting with and destabilizing preformed fibrils.[13,35] Given that amyloid fibrils represent structurally well-defined, persistent assemblies that accumulate during disease progression and serve as nucleation sites for further aggregation, fibrillar assemblies were selected as the primary therapeutic target in this study. By including both Aβ and αSyn inhibitors in the analysis, we were able to compare the peptides with each other and identify potential inhibitors effective against both fibril types. From Table 1, it was observed that most of the peptides share significant homology with their target sequences. In the case of Aβ, the central hydrophobic region Aβ(16–20) serves as a template for designing peptide inhibitors,[15] while for α-synuclein, the core NAC region (residues 64–86) is commonly utilized due to its strong propensity to form β-sheet structures.[37] Additionally, the C-terminal region Aβ(29–42), which can form fibrils independently,[82] represented a key structural fragment for the design of certain sequences.[28,48]

The inhibitory effects on fibril formation were mainly determined by ThT fluorescence assay and circular dichroism spectroscopy. In these studies, most of the peptides reported were in the L-form; however, to enhance their effectiveness, some were designed with N-terminal acetyl, and/or C-terminal amide modification, which has been reported to suppress fibril and oligomer formation and reduce toxicity.[39] In addition, to prevent enzymatic degradation, the incorporation of D-amino acids was proposed as an effective strategy, as demonstrated for the KLVFFA[36] and Dpep[40] inhibitors.

Binding scores of the peptides at the active sites of the proteins, which provide an important measure of binding strength, are summarized in Table 3, where more negative values indicate stronger affinities. Interestingly, according to ADCP docking results, the Pep1.3 peptide, originally developed against αSyn, showed the highest binding score on amyloid-β (2MXU), while KR peptide, designed for amyloid-β, performed best on α-synuclein (2N0A). This intriguing cross-reactivity suggests that peptide inhibitors developed for one neurodegenerative target may also interact effectively with other pathological proteins, highlighting the potential of beta-sheet breaker peptides to be repurposed across different neurodegenerative diseases.

Among the top five peptides based on binding scores, four were common across both targets, revealing a subset of beta-sheet breakers with broad binding potential. Moreover, many peptides originally developed for amyloid-β show substantial binding on α-synuclein, emphasizing the potential to repurpose Alzheimer-targeted beta-sheet breakers for Parkinson's disease and possibly other neurodegenerative disorders.

The top-performing peptides share various common structural features. They are relatively longer (typically 10–12 residues), frequently contain a Phe–Phe (FF) aromatic pair, and exhibit either positive or negative net charge. In contrast, sequences that performed poorly in docking often contained a PGVT-like motif (derived from mutations in the αSyn NAC 69–77 region) or were enriched in apolar residues (V, A, G), suggesting that these features may negatively influence predicted binding affinity. From HPEPDOCK results, it is observed that KR and RR peptides show superior affinity for both targets, having FFARR motif in common and net cationic character. ADCP results are mostly validated by HPEPDOCK predictions, with the exception of Pep1.3. While Pep1.3 ranked among the top performers in ADCP, it exhibited only intermediate binding scores in HPEPDOCK. This discrepancy can be attributed to its unique characteristics: unlike the other top-performing peptides, Pep1.3 lacks aromatic residues (F/Y) and an FF motif. Although its net charge is similar to some sequences (*e.g.*, HKQLPFFEED), the combination of negative residues and absence of aromatic/hydrophobic motifs may likely contribute to its lower binding performance in HPEPDOCK.

During docking, defining a single grid box suitable for all peptides proved challenging, due to their variable lengths, which ranged from 5 to 12 residues. Grid boxes initially set to intermediate sizes (30–45 Å), which are reported in the main text, were suitable for all peptides. However, shorter peptides (5–6 residues) or longer peptides (10–12 residues) could be under- or over-represented in these grids, potentially affecting conformational sampling. In other words, small boxes may be insufficient to accommodate longer peptides (9–12 residues) and their diverse conformations. Larger grids carry the risk of molecules drifting outside the active site or binding to alternative regions of the protein, potentially reducing predictive accuracy. Therefore, to ensure robustness, additional docking calculations were performed using smaller (25 Å) and larger (50 Å) grid boxes, and these results were provided in the SI (Tables S1 and S2). The high degree of concordance in peptide rankings across different grid sizes supports the reliability of the results.

Peptide stability and binding free energies *via* molecular dynamics

Based on their frequency of occurrence among the top-performing peptides, five candidates (Pep1.3, KR, RR, H102, and HPYD), were selected for further stability assessment through MD simulations. The stability of each peptide–protein complex was evaluated by calculating the RMSD of peptide backbone atoms, as shown in Fig. 3a and b.

For the 2MXU systems, the RR and Pep1.3 peptides exhibit relatively stable RMSD values over time, indicating minimal structural changes upon binding. In contrast, RMSD values for the 2N0A systems are generally higher and more variable. Notably, Pep1.3 shows pronounced fluctuations between 0.4 and 0.6 nm, suggesting either increased structural flexibility or lower binding stability. While RR and KR peptides are relatively stabilized in 2N0A, they display even milder fluctuations compared to 2MXU. Overall, these observations indicate that RR exhibits the most prominent binding stability across both systems.

The binding free energy calculations obtained from gmx_MMPBSA (*cf.* Fig. 3(c)) reveal that the KR and RR peptides possess the strongest affinities toward the 2MXU target, with average binding free energies of approximately −59 kJ mol^{-1} and −50 kJ mol^{-1}, respectively. In contrast, the H102, HPYD, and Pep1.3 peptides exhibited weaker (roughly half), and comparable binding free energies ranging from −26 kJ mol^{-1} to −21 kJ mol^{-1}. These findings are consistent with the RMSD analysis, where the more stable peptides (RR and KR) displayed smaller structural fluctuations. This trend was further supported by solvent-accessible surface area (SASA) calculations (Fig. S1), which quantify the interface area between the peptides and their targets. Accordingly, the KR and RR peptides exhibited larger interface areas (∼22 nm^2 and ∼21 nm^2, respectively), whereas the other peptides displayed smaller and comparable areas (∼15 nm^2), implying less favorable peptide–target interactions.

For the 2N0A complexes, the binding free energy values fluctuated substantially, likely due to the instability of peptide positions during the simulations; however, the average binding free energies for KR (−58 kJ mol^{-1}) and RR (−51 kJ mol^{-1}) were consistent with those obtained for the 2MXU systems. Interestingly, Pep1.3 exhibited a relatively high binding energy (−54 kJ mol^{-1}) despite considerable positional variation in its RMSD profile, suggesting that the peptide maintains its interactions through alternating poses rather than a stable conformation. The interface areas of KR and RR in the 2N0A complexes were approximately 23 nm^2 and 19 nm^2, respectively, compared to 13 nm^2 and 12 nm^2 for Pep1.3 and H102. In agreement with its low binding free energy (−28 kJ mol^{-1}), HPYD displayed the smallest interface area (∼9 nm^2). While the absolute binding free energies obtained from MMPBSA should be interpreted with caution, the results reveal consistent relative trends across peptides for both targets, whereby higher binding affinities are generally associated with larger interface areas. This underscores a direct relationship between interfacial contact and peptide–protein stability.[83]

Since KR stands out with its high binding affinity, while RR demonstrates higher structural stability along with a comparable binding free energy, as a final filtering step, we performed blind docking calculations for all five candidates *via* HPEPDOCK. In case of blind docking, RR exhibited superior affinity (Table S3) for both targets. Its HPEPDOCK-derived binding pose was consistent with the ADCP pose, supporting its structural stability and favorable binding free energy. As shown in Fig. S2, the alternative binding pose of RR was also highly stable, yielding a similar average binding free energy of approximately −50 kJ mol^{-1}. Therefore, the RR peptide was

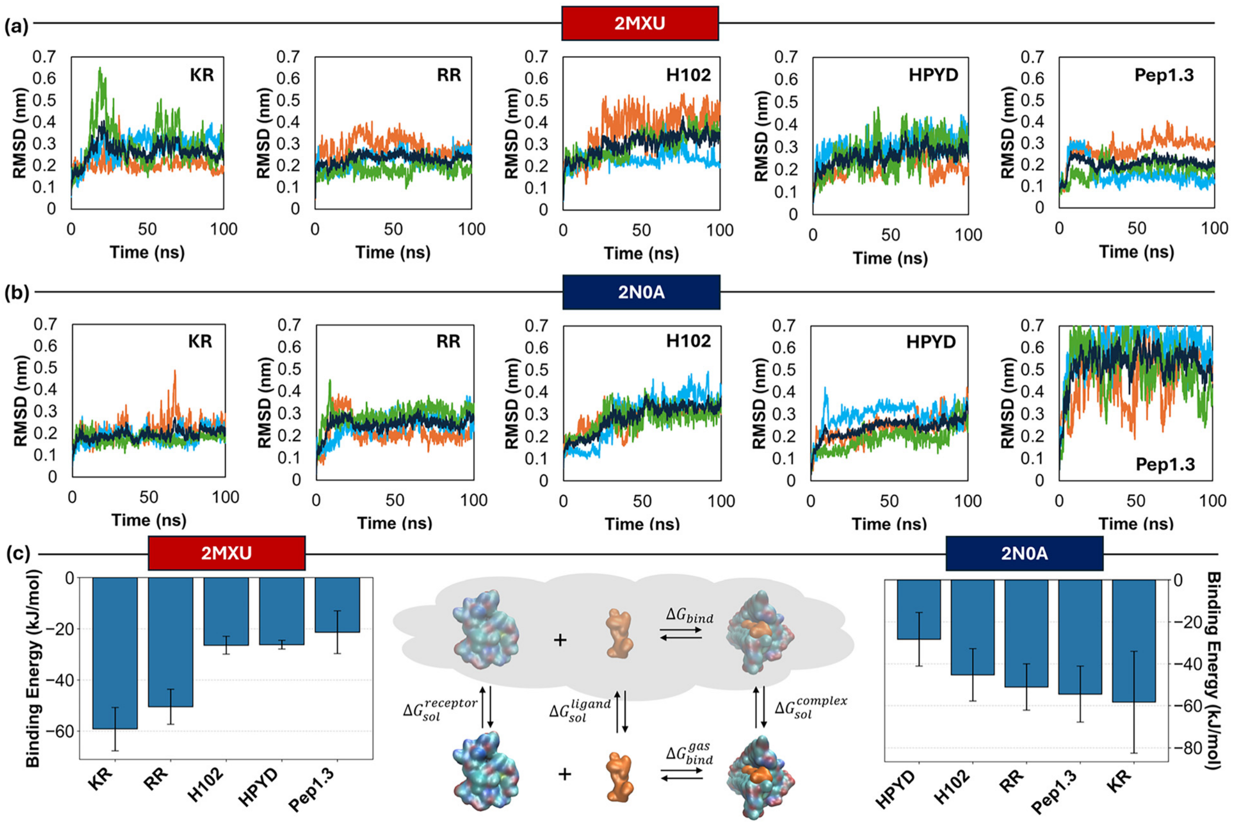

Fig. 3 RMSD profiles of peptide backbone atoms in 2MXU (a) and 2N0A (b) across three independent runs. Black lines represent the average RMSD over three replicas, while green, blue, and orange lines denote individual simulations. The average binding free energies (ΔG_{bind}) of peptides calculated *via* MMPBSA for 2MXU (left) and for 2N0A (right), along with the thermodynamic cycle used for MMPBSA binding free energy calculations (center) (c).

selected for subsequent studies involving liposome interactions and encapsulation potential within lipid nanocarriers.

Peptide–protein molecular interactions

The peptide inhibitor RR was originally designed to bind the 11–23 region of Aβ monomer,[45] whereas most of the studies target hydrophobic 16–20 core to inhibit early aggregation events and the C-terminal 29–42 region to prevent fibrilization.[82] However, in this study, the RR peptide was investigated in the context of fibrillar Aβ instead of its monomeric structure. As a result, the electrostatic interactions previously reported to contribute to binding (involving Glu22 and Asp23) were not observed.[32,45] Instead, hydrogen bonds and hydrophobic interactions were found to dominate the binding interface.

Notably, the hydrogen bonds between Hsd14 (2MXU) and Tyr2/Tyr3 residues, as well as the involvement of the peptide's Phe residues in hydrophobic interactions, were confirmed in this study, highlighting the similarities between monomeric and fibrillar Aβ binding. Additionally, residues Val12, Hsd14, Leu17, Ile32, and Leu34 of Aβ were found to contribute to hydrophobic interactions with the RR peptide (Fig. 4(a)). These findings were consistent with the previous reports showing that replacing the two phenylalanine residues with glycines substantially reduces peptide's inhibitory potency.[45] The restriction of hydrophobic interactions appears to favor the *fast binding–fast dissociating* transient kinetics, suggesting that RR rapidly associates with and dissociates from Aβ without forming a long-lived, stable complex.

For the 2MXU structure, RR was located near the C-terminal region of the protein's β-sheet, adopting a random coil conformation (Fig. 4(b)). The peptide formed hydrogen bonds mainly with Gln15, Leu34, Hsd14, and Gly33, while its Arg (1, 9, and 10) and Tyr (2 and 3) residues acted as hydrogen-bond donors or acceptors. Across all three independent simulation runs, hydrogen bonds with Gln15 exhibited occupancies above 30%, highlighting its central role in binding stability. Previous studies on peptide inhibitors of fibrillar Aβ also emphasized the critical involvement of Hsd14 in the central region and Gly33 and Leu34 in the C-terminal region, underscoring their function for stable peptide binding.[32,84] Furthermore, motifs such as Val12, Hsd14, Ile32, Gly33, and Leu34 are also implicated in partial dissociation of Aβ fibrils, as small molecules or peptides can bind to these residues and processively destabilize the outermost peptide by targeting the 11EVHH14 motif and hydrophobic clusters like Leu17, Phe19, and Ile32.[85]

For the 2N0A structure, the RR peptide adopts a random coil conformation, similar to that in the 2MXU complex, as

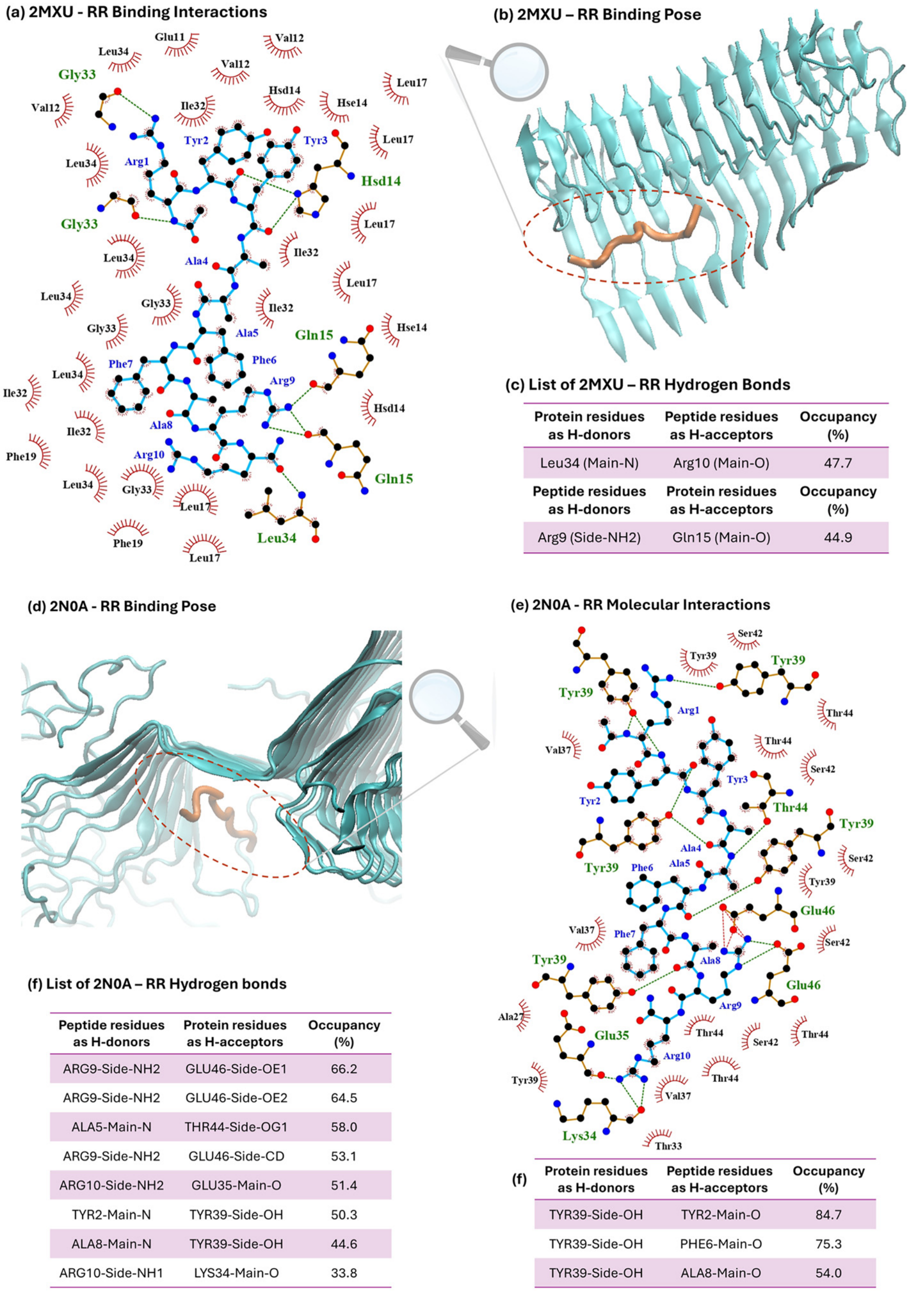

(c) List of 2MXU – RR Hydrogen Bonds

Protein residues as H-donors	Peptide residues as H-acceptors	Occupancy (%)
Leu34 (Main-N)	Arg10 (Main-O)	47.7
Peptide residues as H-donors	**Protein residues as H-acceptors**	**Occupancy (%)**
Arg9 (Side-NH2)	Gln15 (Main-O)	44.9

(f) List of 2N0A – RR Hydrogen bonds

Peptide residues as H-donors	Protein residues as H-acceptors	Occupancy (%)
ARG9-Side-NH2	GLU46-Side-OE1	66.2
ARG9-Side-NH2	GLU46-Side-OE2	64.5
ALA5-Main-N	THR44-Side-OG1	58.0
ARG9-Side-NH2	GLU46-Side-CD	53.1
ARG10-Side-NH2	GLU35-Main-O	51.4
TYR2-Main-N	TYR39-Side-OH	50.3
ALA8-Main-N	TYR39-Side-OH	44.6
ARG10-Side-NH1	LYS34-Main-O	33.8

(f)

Protein residues as H-donors	Peptide residues as H-acceptors	Occupancy (%)
TYR39-Side-OH	TYR2-Main-O	84.7
TYR39-Side-OH	PHE6-Main-O	75.3
TYR39-Side-OH	ALA8-Main-O	54.0

Fig. 4 Molecular interaction maps (a, e), binding modes (b, d), and list of hydrogen bonds (c, f) of the RR peptide in complex with 2MXU and 2N0A, respectively. In binding modes, the peptide is shown in orange, while proteins are displayed in cyan cartoon format. Interaction maps depict hydrogen bonds (green dashed lines), electrostatic interactions (red dashed lines), and hydrophobic contacts (red spoked arcs). Here, peptide residues are shown in blue, and protein residues in green. Among hydrogen-bond lists, only hydrogen bonds with ≥30% occupancy is included to represent stable interactions.

shown in Fig. 4(d). The key interacting residues identified include GLU46, THR44, GLU35, and TYR39 (Fig. 4(e)). Electrostatic interactions are formed between ARG9 of the peptide and GLU46 of the protein, while hydrophobic contacts involving VAL37, SER42, TYR39, and THR44 further contribute to binding stability. Compared to the 2MXU complex, RR forms more stable hydrogen bonds (Fig. 4(f)), with arginine side chains serving as major hydrogen donors. In addition, TYR39 of 2N0A also participates in hydrogen bonding as a donor *via* its side-chain –OH group.

These findings agree with earlier studies demonstrating that small molecule inhibitors of αSyn fibrils (2N0A) at site 2, frequently engage interactions with TYR39 and THR44 residues.[58] More broadly, mutagenesis studies have revealed that aromaticity at position 39 strongly influences both amyloid fibril formation and membrane-bound conformations of αSyn.[86] Thus, αSyn aggregation may be governed not only by its amyloidogenic NAC region, but also by sequence motifs outside the fibril core, highlighting the sequence-specific regulation underlying amyloid-associated toxicity. In this context, recent work on a radioligand targeting αSyn fibrils revealed critical interactions with TYR39, SER42, and THR44, yet also showed measurable binding to Aβ fibrils, emphasizing the challenges in achieving fibril selectivity.[87] Together, the ability of RR to interact effectively with both Aβ and αSyn indicates its potential in terms of the modulation of fibril assembly and stability while motivating further investigation into its selectivity and inhibitory mechanisms beyond its established activity against Aβ aggregation.

Atomistic MD simulations of RR peptides with lipid membranes

To investigate the interactions between the RR peptide and liposomal membranes, we analyzed peptide distribution in both saturated (DMPC) and unsaturated (DOPC) membrane models. To mimic realistic blood circulation conditions, 5% PEGylated lipids were included, and cholesterol (CHOL) was maintained at 0, low (5%) and high (35%) concentrations. The resulting structural and dynamic membrane properties are summarized in Table 4 and were found to be in good agreement with previous reports on bare membranes.[73,88]

In the absence of peptides, it is observed that the condensing effect of CHOL causes a reduction in APM, APL and lateral diffusion values while increasing bilayer thickness.[89–91] The decrease in areas and lateral diffusion is related to the fact that cholesterol promotes order between lipid molecules, and this increased order decreases membrane fluidity, resulting in a thicker bilayer.[73] For DMPC systems, the addition of 35% CHOL decreases APM by approximately 30%, from 0.60 nm^2 to 0.42 nm^2 while in DOPC systems, APM decreases by 26%, from 0.69 nm^2 to 0.51 nm^2. At 5% CHOL, bilayer thickness values remain similar to those in cholesterol-free membranes. Upon increasing CHOL to 35%, bilayer thickness rises from 3.6 nm to 4.4 nm in DMPC and from 3.8 nm to 4.3 nm in DOPC, indicating that CHOL's effect is more pronounced in DMPC membranes, with an approximate 5 : 4 effect ratio compared to DOPC. When the molecular area of cholesterol is also taken into account, the reduction in APL becomes even more pronounced, yielding an approximate 2 : 1 ratio between DMPC and DOPC bilayers.

Regarding lateral diffusion, DMPC bilayers exhibit almost complete restriction at 35% CHOL, whereas DOPC bilayers retain some mobility, consistent with literature.[92] These differences arise because saturated, short-chain lipids like DMPC have higher intrinsic ordering, while in unsaturated, longer-chain lipids like DOPC, cholesterol's effect is limited due to the bending of hydrocarbon tails. Lipid ordering is characterized by the lipid order parameter, which reflects how regularly the hydrophobic tails (sn-1 and sn-2 chains) of lipids are aligned. Consistent with the above findings, Fig. 5 shows a pronounced increase in lipid ordering for both DMPC and DOPC membranes as cholesterol concentration increases. The order parameter of DOPC systems is lower than that of DMPC, primarily due to the presence of a cis double bond at the ninth carbon of DOPC's oleic acid chains. This unsaturation introduces a kink in the hydrocarbon tail, disrupting regular packing and reducing overall chain order.[93]

From Table 4, it can also be seen that, within the timescale of the all-atom simulations, the addition of peptides did not induce significant changes in the areas, thickness and lateral diffusion properties of lipid membranes. Likewise, no notable deviations were observed in the lipid order parameters. These results are consistent with the notion that the peptides predominantly remain at the membrane–aqueous interface rather than penetrating deeply into the bilayer over the simulation durations. On the other hand, the limited simulation time prevents drawing definitive conclusions about their broader structural or dynamical effects on the membranes.

When the simulation trajectories are examined, it is observed that the peptides are mostly embedded within the PEG corona regions, where they interact primarily with the hydrophilic headgroups of the membranes. Such behavior reflects the effect of PEGylation in attenuating peptide–lipid interactions by steric and hydrophilic shielding of membrane-active residues, thereby disfavoring membrane insertion.[94,95] In DMPC bilayers, peptides are more prone to aggregation than in DOPC systems. The final simulation snapshots at 400 ns (Fig. 6) illustrate that peptides predominantly form triple

Table 4 Membrane properties in the absence and presence of RR peptide

Model bilayer	Area per molecule (nm^2)	Area per lipid (nm^2)	Bilayer thickness (nm)	Lipid (P atom) lateral diffusion constant (μm^2 s^{-1})
DMPC/DMPE_PEG	0.601 ± 0.009	0.601 ± 0.009	3.61 ± 0.04	7.9 ± 0.6
DMPC/DMPE_PEG/RR	0.604 ± 0.008	0.604 ± 0.008	3.59 ± 0.04	9.4 ± 1.8
DMPC/DMPE_PEG/CHOL5	0.567 ± 0.008	0.575 ± 0.008	3.73 ± 0.04	7.3 ± 0.1
DMPC/DMPE_PEG/CHOL5/RR	0.570 ± 0.007	0.579 ± 0.008	3.71 ± 0.04	7.5 ± 0.2
DMPC/DMPE_PEG/CHOL35	0.415 ± 0.003	0.429 ± 0.003	4.39 ± 0.02	0.6 ± 0.4
DMPC/DMPE_PEG/CHOL35/RR	0.412 ± 0.003	0.424 ± 0.003	4.41 ± 0.02	0.6 ± 0.6
DOPC/DOPE_PEG	0.687 ± 0.008	0.687 ± 0.008	3.83 ± 0.04	10.0 ± 2.2
DOPC/DOPE_PEG/RR	0.692 ± 0.009	0.692 ± 0.009	3.82 ± 0.04	10.6 ± 1.3
DOPC/DOPE_PEG/CHOL5	0.659 ± 0.010	0.673 ± 0.010	3.90 ± 0.05	9.9 ± 1.3
DOPC/DOPE_PEG/CHOL5/RR	0.661 ± 0.009	0.675 ± 0.010	3.89 ± 0.04	9.4 ± 1.1
DOPC/DOPE_PEG/CHOL35	0.507 ± 0.006	0.569 ± 0.006	4.33 ± 0.04	6.5 ± 0.3
DOPC/DOPE_PEG/CHOL35/RR	0.508 ± 0.006	0.571 ± 0.006	4.32 ± 0.04	7.6 ± 3.9

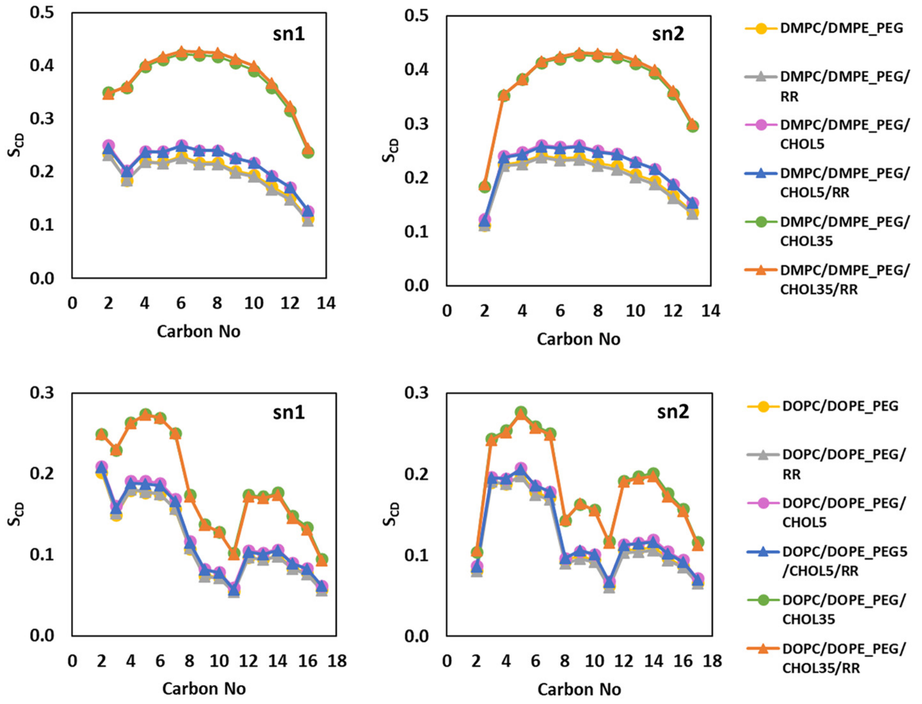

Fig. 5 Lipid order parameters of the sn1 (left) and sn2 (right) acyl chains in DMPC and DOPC bilayer systems.

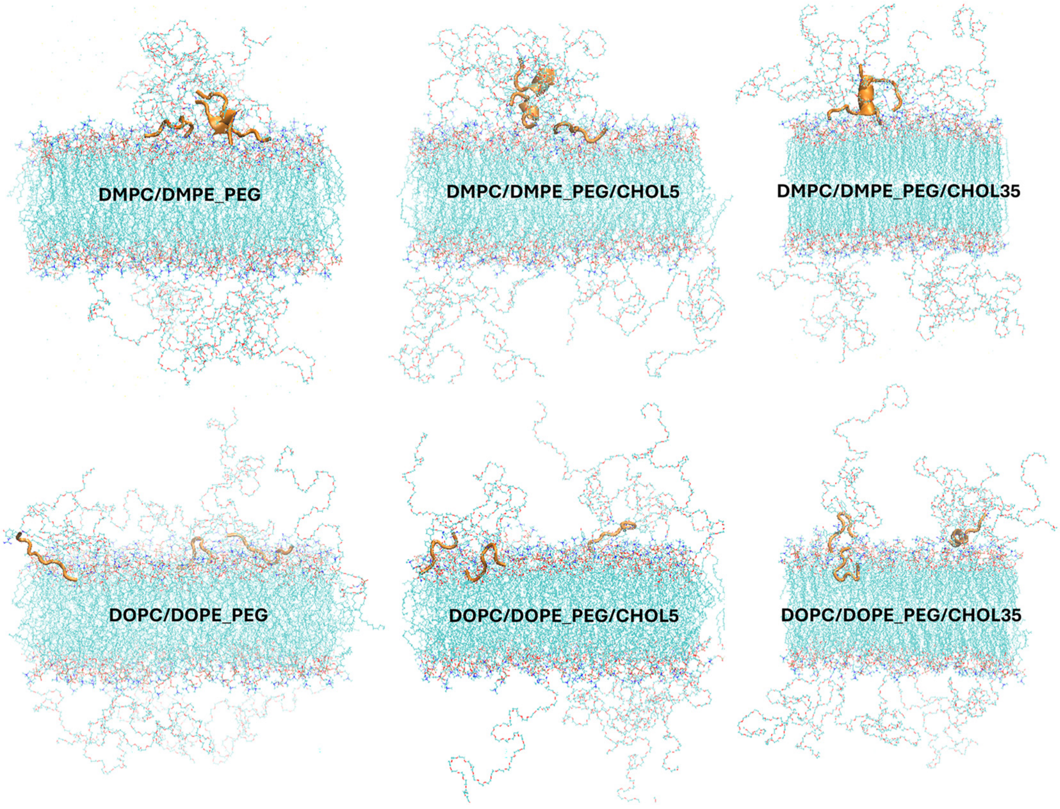

Fig. 6 Distribution of the RR peptide in different membrane models. Snapshots were taken at 400 ns of the simulation trajectories. The RR peptide is shown in orange with cartoon representation, while PEGylated bilayers are displayed by atom type using line representation.

aggregates in DMPC, while they are mostly dispersed or form dimeric clusters in DOPC. This aggregation pattern can be attributed to the higher packing density of DMPC bilayers which restrict peptide diffusion and promote intermolecular association at the membrane surface. A comparable organization was reported for melittin, which forms oligomers in simple PC membranes but shows reduced aggregation in complex bacterial or plasma membranes, particularly when interacting with GM3 gangliosides.[96] These findings suggest that the aggregation and organization of peptides are influenced by the lipid environment, with membrane packing and local interactions governing whether peptides remain dispersed or assemble into higher-order oligomers.

To assess the compactness of PEG upon peptide addition, the radii of gyration (R_g) of PEG chains in the upper and lower leaflets were calculated, and the average values are presented in Fig. 7(a). Here, it is worth mentioning that each PEG chain is covalently attached to a lipid molecule at one end, leaving only the distal end free. Therefore, the R_g values provide insight into the conformational arrangement of PEG chains on the membrane surface. Since the conformational flexibility of PEG also depends on the nature of the underlying lipid, PEG chains tend to adopt more compact conformations on less fluid membranes such as those composed of DMPC, whereas they are more extended on highly fluid bilayers like DOPC. Consistent with these characteristics, in all cases, the PEG chains exhibited smaller radii of gyration in the upper leaflet, where the peptides were located. In contrast, the lower leaflet, which did not directly interact with the peptides, displayed less compact PEG conformations. Moreover, as membrane permeability to peptides increased, the compactness of the PEG chains decreased. These results indicate that the PEG chains adopt a more compact configuration when the peptides primarily interact with the PEG moieties. On the other hand, when peptide–lipid interactions become dominant or peptide penetration into the membrane increases, the PEG chains exhibit more extended and dispersed conformations.

This trend is supported by the center-of-mass distance between peptide RR and the membrane, which serves as an indicator of peptide insertion depth (Fig. 7(b)). In DMPC/DMPE_PEG system, peptides remained relatively closer to the membrane surface with an average COM distance of ~2.6 nm, whereas the inclusion of cholesterol increased this distance to ~3.1 nm, indicating reduced peptide insertion (Table S4). This reduced insertion depth correlates with a decrease in the R_g of PEG chains, suggesting a more compact PEG conformation. Conversely, the highest R_g were observed in the DOPC/DOPE_PEG membrane, where the peptides exhibited the smallest COM distance (~2.4 nm), corresponding to the greatest peptide insertion. A gradual increase in the COM distance upon cholesterol addition (~2.4 nm for CHOL5 and ~2.8 nm for CHOL35) was accompanied by reduced peptide permeability and more compact PEG conformations.

To better understand molecular-level interactions, hydrogen bonds formed by the peptides with the membrane and PEG groups were examined, and the bond distributions were shown

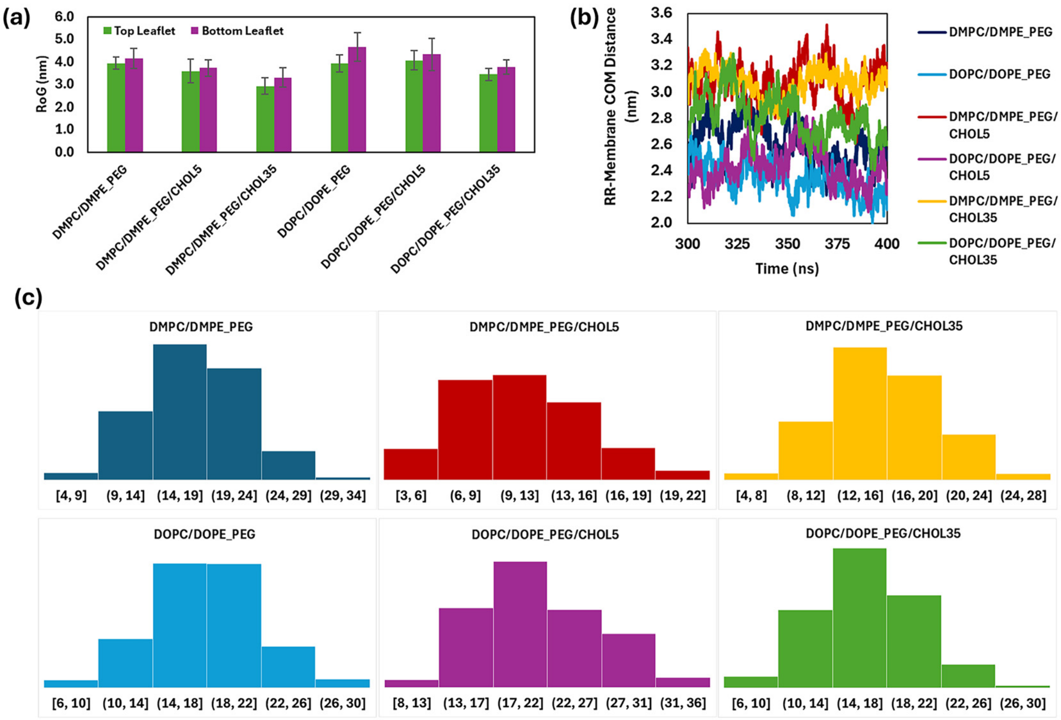

Fig. 7 Average radius of gyration (RoG) of PEG chains from PE lipids in the upper and lower leaflets of the bilayer (a), average center-of-mass (COM) distance between the RR peptide and membrane during the last 100 ns of simulations for different membrane models (b), hydrogen bond distributions formed between the peptide and lipids across different membrane models (c).

in Fig. 7(c) with histograms. Accordingly, it appears that the highest number of hydrogen bonds occurred with the DOPC membrane at 0% and 5% CHOL, whereas the corresponding H-bonds with PEG were at their lowest levels in these two cases (*cf.* Fig. S3). From hydrogen bonding analysis, it was also observed that peptides formed a relatively high number of hydrogen bonds with lipids (17–21 on average) in DOPC systems, whereas in DMPC membranes the number was lower (11–18). Correspondingly, peptide–PEG hydrogen bonds were minimal in both cases, but slightly fewer in DOPC systems (2–3) compared to DMPC (4–6), confirming that when peptides engage more extensively with the membrane, their interactions with PEG are reduced. These results indicate that peptide–lipid H-bond interactions dominate over peptide–PEG interactions and that membrane composition modulates the distribution of hydrogen bonding, with potential implications for peptide anchoring and stability in different lipid environments. The limited hydrogen bonding between peptides and PEG chains further suggests that their interactions could possibly be driven by van der Waals forces rather than hydrogen bonds.

Overall, hydrogen bonding analysis highlighted the peptide–lipid interactions across different membrane models, however, to gain further insight into these interactions at the atomic level, the specific atom groups involved in peptide–lipid hydrogen bonds were analyzed and presented in Table 5. The analysis revealed that in all stable hydrogen bonds, the RR peptide acted as the hydrogen donor, while the PC and PE lipids served as the hydrogen acceptors. A more detailed examination showed that the majority of hydrogen bonds were formed between the guanidinium groups of Arginine (Arg) residues and the oxygen atoms of the phosphate groups (O13, O14) in the lipids. Thus, the most frequently observed hydrogen bond involved the Arg residue at position 9, followed by other Arg residues located at the terminal regions of the peptides. In addition to Arg, Tyr and Ala residues also participated in hydrogen bonding through their backbone amide (–NH) groups, albeit to a lesser extent. Notably, the –NH groups in the Arg side chains acted predominantly as hydrogen donors, consistent with the well-known ability of Arg residues to interact directly with anionic phosphate headgroups and polar regions through strong cationic charge interactions and multiple hydrogen bonds.[97,98] Furthermore, the multidentate hydrogen-bonding capacity of Arg residues allows them to interact simultaneously with more than one phosphate group,[97] as shown in Fig. S4.

The density distribution profiles in Fig. 8 indicate that as cholesterol content increases, the water density profile extends further from the membrane center, while the PEG and phosphorus (P) peaks become sharper in DMPC membranes. This confirms that cholesterol leads to a more ordered lipid arrangement and reduces water penetration into the membrane region. A similar trend is observed in DOPC membranes;

Table 5 Key amino acid residues involved in hydrogen bonds between peptides and lipids. The results are based on hydrogen bonds with an occupancy above 30% during the last 100 ns of the simulation trajectories

Lipid composition	Amino acids involving in hydrogen bonding	Hydrogen acceptor atoms of lipids
DMPC/DMPE_PEG	Tyr2, Arg10, Arg1, Arg9	O14, O13, O11
DMPC/DMPE_PEG/CHOL5	Arg9, Arg10, Ala8	O13, O14
DMPC/DMPE_PEG/CHOL35	Arg10, Arg9, Tyr3, Arg1	O13, O11, O14, O12
DOPC/DOPE_PEG	Arg10, Tyr2, Ala5, Arg9	O14, O32, O13
DOPC/DOPE_PEG/CHOL5	Arg1, Tyr2, Arg9, Tyr3	O14, O13
DOPC/DOPE_PEG/CHOL35	Arg9, Arg1, Arg10	O14, O13

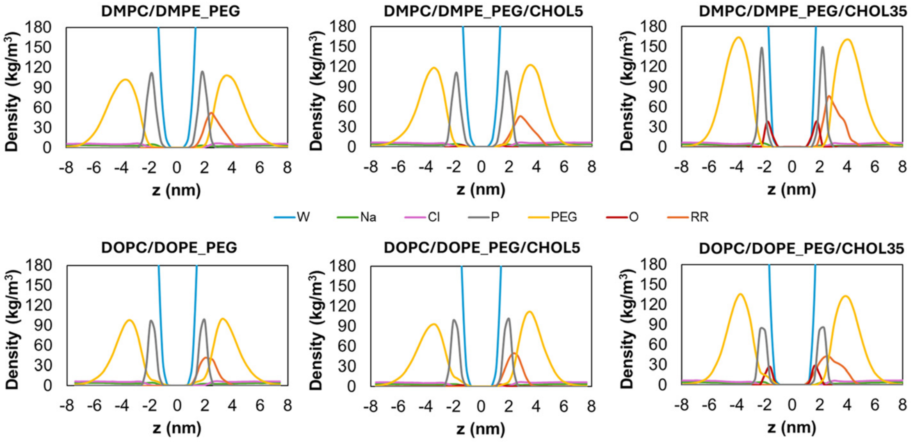

Fig. 8 Density distributions of water (W), ions (Na and Cl), phosphorus (P), polyethylene glycol (PEG), oxygens (O) of cholesterol and peptide (RR) in DMPC and DOPC membrane systems.

however, in this case, the phosphorus density profile becomes markedly less pronounced at 35% cholesterol. This difference implies that cholesterol induces a less compact organization in DOPC membranes compared to DMPC. Furthermore, the profiles confirm that the peptides are mainly positioned near the headgroups of the upper leaflet, and at higher cholesterol levels, they tend to spread more into the bulk solvent region.

To investigate the effect of peptides on ion distribution, density profiles were demonstrated more closely at Fig. 9. It was observed that the peak symmetries of Na^+ and Cl^- ions are significantly perturbed with the addition of peptides. It is particularly noteworthy that Na^+ ion density decreases in the upper leaflet where the peptides are located. This observation can be associated with the electrostatic repulsion sourced by the cationic Arg side chains of RR peptide, displacing Na^+ ions away from the peptide-rich region. In cholesterol-containing systems, Na^+ ions were found to be more concentrated in the lower leaflet while negatively charged ions were preferentially localized in the upper leaflet (*cf.* Fig. S5). In contrast, a more symmetrical distribution of Cl^- ions was observed across both leaflets in the absence of cholesterol. Taken together, two major conclusions can be drawn: (i) the presence of cationic peptides in the upper leaflet restricts the direct interaction of ions with the membrane surface, leading to the attraction of Cl^- ions and repulsion of Na^+ ions; and (ii) the increased interaction area on the membrane surface in the lower leaflet facilitates a denser accumulation of Na^+ ions in that region.

Coarse-grained self-assembly of lipids with RR peptides

Coarse-grained MD simulations are essential for capturing the dynamic evolution of complex systems over realistic timescales, enabling the exploration of long-term behavior that is often inaccessible at the atomistic level.[99] Although the reduced resolution of coarse-grained models limits direct quantitative mapping between atomistic descriptors and coarse-grained observables, consistent trends can nonetheless be identified across scales. In this study, the self-assembly behavior of lipids was investigated at the coarse-grained level, both in the absence and presence of the RR peptide, to complement atomistic analyses by capturing long-timescale trends in peptide–lipid interactions and membrane association relevant to potential future encapsulation studies. Since atomistic simulations revealed no significant differences between the 5% CHOL and cholesterol-free systems, the coarse-grained systems were carried out at 0%, 15%, and 35% CHOL concentrations.

Accordingly, the time-dependent structural evolution of the systems in the absence and presence of peptides is illustrated in Fig. 10 and 11, respectively. As shown in Fig. 10, in the DLPC/DLPE-PEG system, small local clusters and bilayers formed rapidly and transformed into larger bilayer sheets and vesicular systems of various sizes within approximately 2 µs. After 10 µs, a bilayer and two liposome vesicles of ∼17 nm in diameter was formed. In systems containing 15% CHOL, bilayer and nanodisc structures appeared within 2 µs, but after 10 µs, these structures evolved into vesicles of ∼15–17 nm in diameter, similar to the cholesterol-free system. Remarkably, at 35% CHOL, the bilayers coalesced into a large nanodisc structure that did not transition into a closed vesicle. These findings indicate that the presence of cholesterol in DLPC systems slows down the self-assembly process and, and at high cholesterol levels (35%), lipids become trapped in a metastable nanodisc state. This behavior can be attributed to reduced structural rearrangements arising from decreased bilayer flexibility in the presence of cholesterol.[100]

When the effect of peptide addition on lipid self-assembly was examined (Fig. 11), lipids exhibited a stronger tendency to aggregate in systems with low cholesterol content. In contrast to the small and heterogeneous bilayer patches observed in peptide-free systems within 1 µs, the presence of the RR peptide led to the formation of larger disk-like aggregates that subsequently transformed into vesicles within ∼2 µs. This behavior can be attributed to the positively charged RR peptide, which lowers surface energy by establishing electrostatic interactions with lipid headgroups, thereby facilitating closer lipid packing and promoting more stable interfaces. In this way,

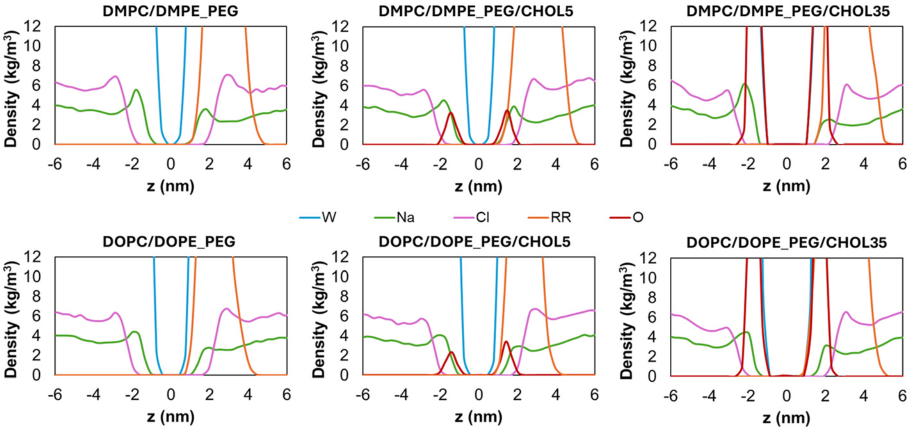

Fig. 9 The magnified view of density distributions of water (W), ions (Na and Cl), oxygens (O) of cholesterol and peptide (RR) in DMPC and DOPC membrane systems.

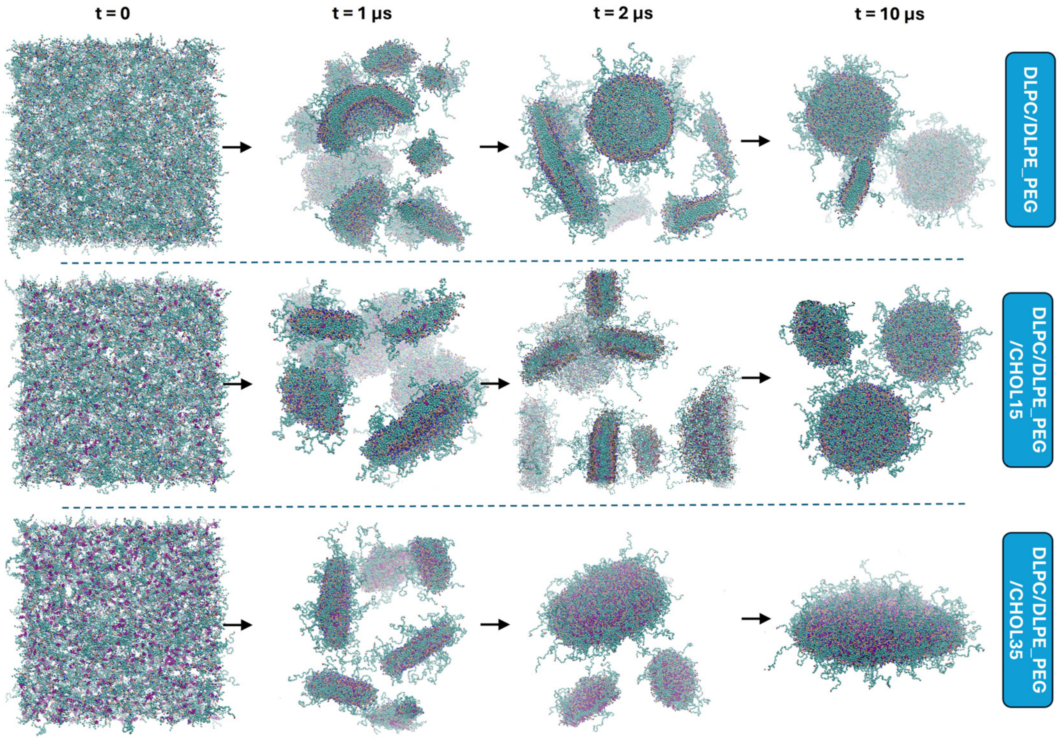

Fig. 10 The self-assembly process of lipids over time in the absence of peptides. Water and ion molecules are not shown for clarity.

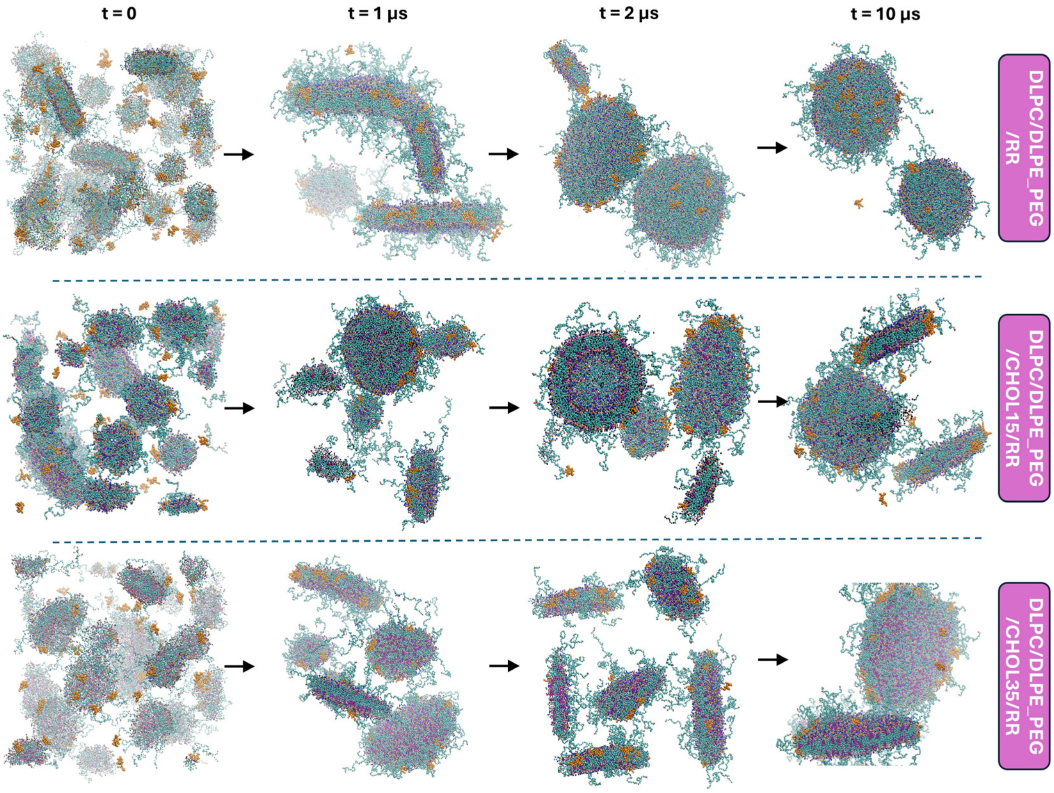

Fig. 11 The self-assembly process of lipids over time in the presence of RR peptides. Water and ion molecules are not shown for clarity. RR peptides are represented by orange van der Waals spheres.

peptides act as molecular bridges that accelerate lipid self-assembly (Fig. S6).

At 35% CHOL, however, increased ordering of lipids prevented vesicle formation even after 10 μs and maintained a lamellar organization. At low CHOL, bilayers or nanodiscs can readily close into vesicles, whereas at high CHOL, the bilayer becomes more rigid and trapped in lamellar or nanodisc states. Due to reduced bilayer curvature ability,[101] the transition to a spherical vesicle becomes thermodynamically unfavorable.

When the spatial distribution of peptides was examined, they were generally found to be embedded among the lipid headgroups and localized around the outer surfaces of the liposomal structures in all systems. This observation is consistent with the behavior seen in atomistic simulations, suggesting that the peptides preferentially interact with lipid headgroups within the inner core or outer water–bilayer interface regions (Fig. 12(a)). Notably, the peptides exhibited no tendency to form large clusters or aggregates with each other.

To characterize peptide–lipid interactions, peptide–phosphate (PO_4^-) radial distribution functions (RDFs) were calculated and shown in Fig. 12(b). The sharp peak around ~0.5 nm indicates close contact between the peptides and the phosphate groups, whereas the broader secondary peak at ~0.93 nm corresponds to neighboring headgroups, suggesting that peptides are, on average, distributed around adjacent lipid headgroups. In Fig. 12(c and d), residue-based peptide–PO_4^- RDFs computed at both atomistic and coarse-grained scales reveal that arginine residues exhibit the highest propensity for lipid interactions, indicating their dominant role in membrane association. This behavior arises from the strong electrostatic attraction and hydrogen-bonding capability of the arginine with the negatively charged phosphate moieties of lipids as explained before. Thus, peptide binding to the membrane is primarily mediated through N- or C-terminal arginine residues, which act as anchoring points and stabilize peptide positioning at the membrane interface across both simulation resolutions.

To further understand the interactions of peptides with lipids, the average number of contacts for each lipid type within 0.6 nm was quantified and presented in Fig. 13(a). In the DLPC/DLPE-PEG system, peptides initially formed extensive contacts with DLPC lipids, which gradually decreased over time in favor of DLPE contacts. Specifically, the proportion of DLPC contacts decreased from 66% at the beginning of the simulation to 37% at 10 μs, while DLPE contacts increased from 34% to 63%. A similar trend was observed in the 15% CHOL system, where DLPC contacts declined from 43% to 24%, and DLPE contacts rose from 45% to 70%. In the 35% CHOL system, due to the lower DLPC content, peptide–DLPC interactions remained relatively limited and stabilized around 26%. Meanwhile, peptide contacts with DLPE and CHOL reached 69% and 5%, respectively, comparable to the 15% CHOL system. These results indicate that cholesterol promotes peptide association with DLPE lipids, while the total number of peptide–cholesterol contacts remain largely unaffected by cholesterol concentration.

In comparison to CG findings, peptide–lipid contacts were also quantified at the atomistic scale for the DMPC/DMPE_PEG and DMPC/DMPE_PEG/CHOL35 systems (Fig. S7) and it was confirmed that peptides more favorably interact with PEGylated PE lipids (%74) than zwitterionic PC lipids (%26), and the inclusion of 35% cholesterol promotes peptide–PE interactions by approximately 10%. While a direct quantitative comparison between the two scales is precluded by CG model limitations and differences in system specifications that

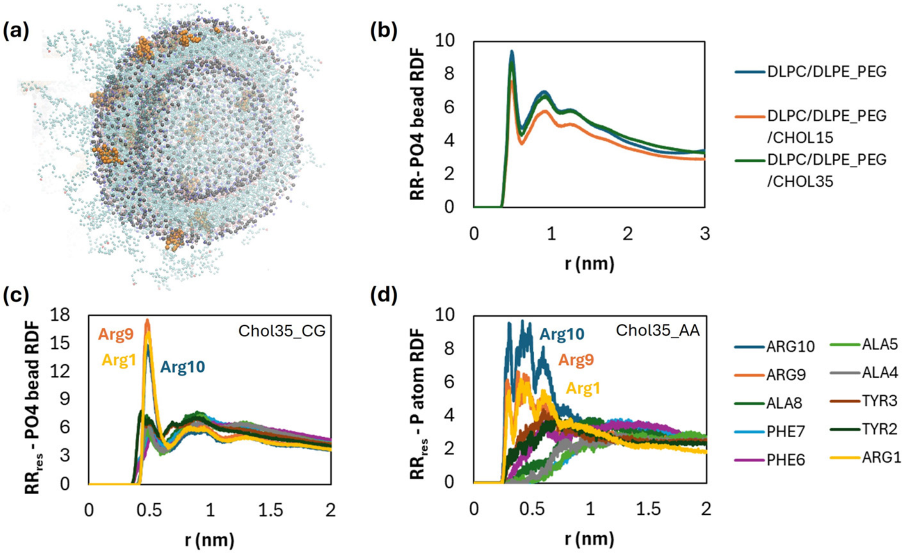

Fig. 12 RR peptide (orange spheres) translocation with respect to phosphate (PO4) beads (gray spheres) (a), the radial distribution function (RDF) of RR peptides relative to PO4 beads (b), residue-based RDF profile of RR relative to PO4 beads at the coarse-grained (CG) level (c) and residue-based RDF profile of RR relative to phosphorus (P) atoms at the all-atom (AA) level (d) for PC/PE_PEG/CHOL35 systems.

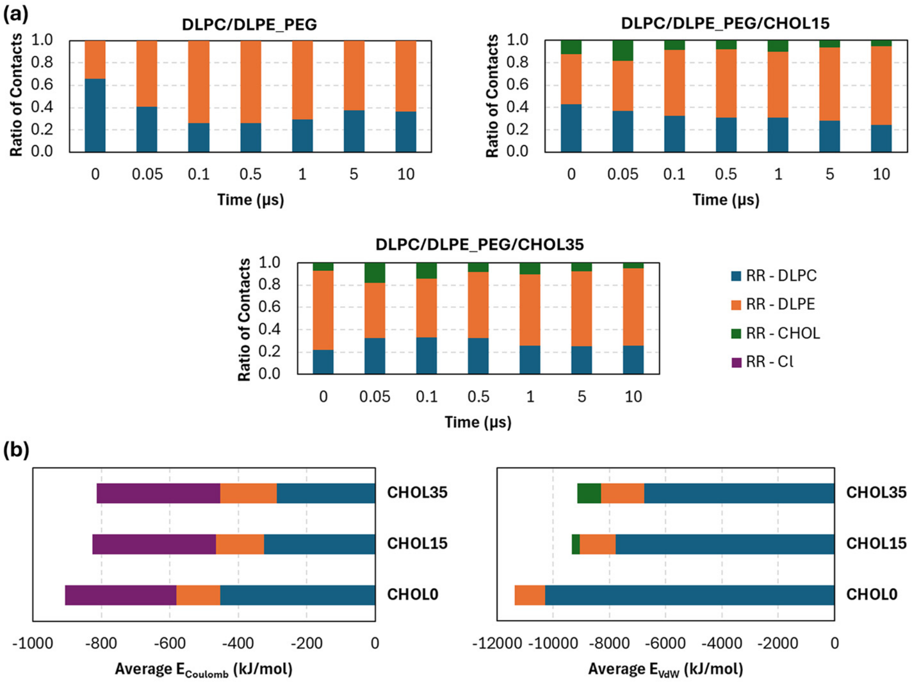

Fig. 13 Normalized contact ratios of RR peptides with lipid molecules within 0.6 nm distance over time (a). Average non-bonded interaction energies between RR peptides and lipid or ion components (b).

modulate peptide localization, the consistency of these relative trends across scales supports the robustness of the observed interaction behavior.

Coulombic and van der Waals (VdW) energy distributions are shown in Fig. 13(b) to compare the short-range nonbonded interactions established between the RR peptide and surrounding components. The total nonbonded interaction energy between the peptides and membrane molecules was higher in the absence of cholesterol ($\sim-12\,000$ kJ mol^{-1}), whereas reduces with cholesterol addition (~-9500 kJ mol^{-1} and ~-8800 kJ mol^{-1}, respectively). As the cholesterol content increased, both the Coulombic and VdW interaction energies between the peptide and DLPE lipids increased, indicating that peptide–DLPE interactions are favored in cholesterol-containing systems. In contrast, peptide–cholesterol interactions showed an opposite trend: coulombic energies increased, while VdW contributions decreased. This was attributed that cholesterol reorganizes the membrane surface to expose more DLPE headgroups for electrostatic interactions. The electrostatic interactions between the peptides and chloride (Cl^-) ions were found to be slightly stronger in the presence of cholesterol but remained largely independent of cholesterol concentration. Indeed, the average peptide–Cl^- Coulombic energy was approximately -360 kJ mol^{-1} in both the 15% and 35% CHOL systems.

Finally, atomistic analyses of short-range non-bonded energies between peptides and individual lipid components were conducted to evaluate cross-scale consistency (Fig. S8). Despite differences in resolution that make direct comparison between atomistic and coarse-grained observables challenging, both scales reveal comparable cholesterol-dependent behavior, characterized by reduced overall peptide–membrane non-bonded interactions and enhanced peptide affinity for PE lipids.

Conclusion

In conclusion, β-sheet breaker peptides reported in the literature were screened for their binding characteristics against targets associated with Alzheimer's and Parkinson's diseases. Following a comprehensive analysis, the cationic RR peptide was selected for further investigation of its interactions with various lipid-based carrier systems at multiple levels of resolution. The main findings of the present study are summarized as follows:

- Molecular docking and dynamics studies displayed that KR peptides exhibit highest binding free energy to neurological targets while RR has comparable binding energy with greater stability.
- Atomistic MD simulations revealed that RR peptides are embedded within the PEG layers at the water–membrane interface and interact with the lipid headgroups.
- Peptide penetration was found to be more favorable in DOPC membranes compared to DMPC, which has shorter and more saturated hydrocarbon chains.
- Peptide–lipid interactions were predominantly mediated by hydrogen bonds formed between the side chains of arginine (Arg) residues in the peptide and the oxygen atoms of the lipid phosphate groups.

- Self-assembly simulations demonstrated that DLPC/DLPE_PEG systems evolved into vesicular structures in the presence of 0/15% CHOL, whereas at 35% CHOL, a stable nanodisc was formed, indicating that higher cholesterol levels hinder lipid reorganization and bilayer-to-vesicle transition.
- Over the course of the simulations, peptides were found to surround lipid membranes, vesicles, or disk structures externally and interact mostly with the lipid phosphate groups, without diffusing into the inner regions of the liposomes.
- Non-bonded interactions were particularly favored with PEGylated PE lipids, and this effect became more pronounced with increasing cholesterol content.

Collectively, these findings indicate that liposomal formulations containing low cholesterol (0–15%) and incorporating PEG functionalization provide a more favorable environment for cationic peptide association. However, since the peptides preferentially remain at the membrane surface rather than penetrating across the bilayer in our MD simulations, we hypothesize that passive loading may result in surface entrapment or partial encapsulation of peptides, thereby reducing the overall loading yield and stability of the formulation. Consequently, active loading strategies may be preferred to achieve higher encapsulation efficiencies compared to passive methods.[102] In light of the growing evidence between post-COVID-19 conditions and accelerated neurodegeneration, these results offer a molecular-level framework for developing liposome-based peptide therapeutics capable of targeting multiple misfolded protein pathologies.

Author contributions

Gulsah Gul: conceptualization, data curation, formal analysis, funding acquisition, investigation, methodology, project administration, resources, supervision, validation, visualization, writing – original draft, writing – review & editing.

Conflicts of interest

There are no conflicts to declare.

Data availability

The data supporting this article have been included as part of the supplementary information (SI). Supplementary information: binding energy scores of β-sheet breaker peptides obtained from molecular docking using AutoDock CrankPep (ADCP) with a small grid box size of 25 × 25 × 25 Å (Table S1); binding energy scores of β-sheet breaker peptides obtained from molecular docking using AutoDock CrankPep (ADCP) with a large grid box size of 50 × 50 × 50 Å (Table S2); the average protein–peptide interface area values for 2MXU (left) and 2N0A (right) with standard deviations calculated from three independent runs (Fig. S1); HPEPDOCK blind docking results of selected five peptides for stability tests (Table S3). RMSD plots for RR peptide in complex with 2MXU (a), where initial configuration was obtained from ADCP docking calculations. The average binding free energy of RR calculated using MMPBSA based on three independent simulation runs (b) (Fig. S2); the distribution of hydrogen bonds between the RR peptide and PEG chains in different membrane models during the last 100 ns of the simulations (Fig. S3); multidentate hydrogen-bonding behavior of arginine (Arg) residues showing interactions between the NH groups of Arg side chains and the oxygen atoms of phosphate groups in DMPC lipids. The snapshot was taken from the DMPC/DMPE_PEG system at t = 400 ns (Fig. S4); time-averaged center-of-mass (COM) distance of RR peptides from the membrane COM during the last 100 ns of the trajectories (Table S4); spatial distribution of sodium (green) and chloride (pink) ions in the DMPC/DMPE_PEG/CHOL35 membrane system. Peptides are shown in orange cartoon representation (Fig. S5); a self-assembly snapshot illustrating the bridging potential of peptides in the DLPC/DLPE_PEG/CHOL15 system (Fig. S6). Average normalized contact ratios of RR peptides with lipid molecules within 0.4 nm distance in DMPC/DMPE_PEG and DMPC/DMPE_PEG/CHOL35 atomistic membrane systems (Fig. S7). Average short-range non-bonded interaction energies between RR peptides and lipid components in DMPC/DMPE_PEG and DMPC/DMPE_PEG/CHOL35 atomistic membrane systems (Fig. S8). See DOI: https://doi.org/10.1039/d5nr05060j.

Acknowledgements

The financial support was provided by the TÜBİTAK 2218 – National Postdoctoral Research Fellowship Program with the Project No.: 123C377. Computing resources used in this work were mainly provided by the National Center for High Performance Computing of Turkey (UHeM) under grant number 1017912024. Computations were partially performed at the MareNostrum 5 preexascale supercomputing system. The author gratefully acknowledges the Barcelona Supercomputing Center (BSC) and the Scientific and Technological Research Council of Turkey (TÜBİTAK) for providing access to these resources and supporting this research. The author also thanks Dr Erkan Şenses and Dr Erdal Aydın from Koç University for sharing their computational resources without hesitation.

References

1 W. Poewe, K. Seppi, C. M. Tanner, G. M. Halliday, P. Brundin, J. Volkmann, A. E. Schrag and A. E. Lang, Parkinson Disease, *Nat. Rev. Dis. Primers*, 2017, **3**, 1–21, DOI: 10.1038/nrdp.2017.13.

2 D. S. Knopman, H. Amieva, R. C. Petersen, G. Chételat, D. M. Holtzman, B. T. Hyman, R. A. Nixon and D. T. Jones, Alzheimer Disease., *Nat. Rev. Dis. Primers*, 2021, 7(1), 1–21, DOI: 10.1038/s41572-021-00269-y.

3 S. Wang, Y. Jiang, A. Yang, F. Meng and J. Zhang, The Expanding Burden of Neurodegenerative Diseases: An Unmet Medical and Social Need, *Aging Dis.*, 2024, **16**(5), 2937–2952, DOI: 10.14336/ad.2024.1071.

4 G. B. Irvine, O. M. El-Agnaf, G. M. Shankar and D. M. Walsh, Protein Aggregation in the Brain: The Molecular Basis for Alzheimer's and Parkinson's Diseases, *Mol. Med.*, 2008, **14**(7–8), 451–464, DOI: 10.2119/2007-00100.Irvine.

5 P. Kurosinski, M. Guggisberg and J. Götz, Alzheimer's and Parkinson's Disease - Overlapping or Synergistic Pathologies?, *Trends Mol. Med.*, 2002, **8**(1), 3–5, DOI: 10.1016/S1471-4914(01)02246-8.

6 A. Xie, J. Gao, L. Xu and D. Meng, Shared Mechanisms of Neurodegeneration in Alzheimer's Disease and Parkinson's Disease, *BioMed Res. Int.*, 2014, **2014**, 648740, DOI: 10.1155/2014/648740.

7 D. Caligiore, F. Giocondo and M. Silvetti, The Neurodegenerative Elderly Syndrome (NES) Hypothesis: Alzheimer and Parkinson Are Two Faces of the Same Disease, *IBRO Neurosci. Rep.*, 2022, **13**, 330–343, DOI: 10.1016/j.ibneur.2022.09.007.

8 L. C. Serpell, Alzheimer's Amyloid Fibrils: Structure and Assembly, *Biochim. Biophys. Acta, Mol. Basis Dis.*, 2000, **1502**(1), 16–30, DOI: 10.1016/S0925-4439(00)00029-6.

9 J. Burré, M. Sharma and T. C. Südhof, Definition of a Molecular Pathway Mediating α-Synuclein Neurotoxicity, *J. Neurosci.*, 2015, **35**(13), 5221–5232, DOI: 10.1523/JNEUROSCI.4650-14.2015.

10 X. Y. Du, X. X. Xie and R. T. Liu, The Role of α-Synuclein Oligomers in Parkinson's Disease, *Int. J. Mol. Sci.*, 2020, **21**(22), 1–17, DOI: 10.3390/ijms21228645.

11 I. B. Bruinsma, A. Karawajczyk, G. Schaftenaar, R. M. W. De Waal, M. M. Verbeek and F. L. Van Delft, A Rational Design to Create Hybrid β-Sheet Breaker Peptides to Inhibit Aggregation and Toxicity of Amyloid-β, *MedChemComm*, 2011, **2**(1), 60–64, DOI: 10.1039/c0md00213e.

12 A. T. Mullin, S. A. Michelhaugh, B. R. Fitzgerald, J. E. Barnes, M. J. Calcaterra and S. A. Petty, Capped Gly-Gly-Ala Inhibits Β–sheet Formation and Aggregation in Peptides Associated with Neurodegenerative Disease, *Vib. Spectrosc.*, 2020, **111**, 103168, DOI: 10.1016/j.vibspec.2020.103168.

13 C. Soto, M. S. Kindy, M. Baumann and B. Frangione, Inhibition of Alzheimer' s Amyloidosis by Peptides That Prevent b-Sheet Conformation 1 Design of Inhibitor Peptides We Focused on the Central Hydrophobic Region within the N-Terminal Domain of Ab Amino, *Biochem. Biophys. Res. Commun.*, 1996, **226**, 672–680.

14 C. Soto, E. M. Sigurdsson, L. Morelli, R. A. Kumar, E. M. Castaño and B. Frangione, β-Sheet Breaker Peptides Inhibit Fibrillogenesis in a Rat Brain Model of Amyloidosis: Implications for Alzheimer's Therapy, *Nat. Med.*, 1998, **4**(7), 822–826, DOI: 10.1038/nm0798-822.

15 L. O. Tjernberg, J. Näslundt, F. Lindqvist, J. Johansson, A. R. Karlström, J. Thyberg, L. Tereniust and C. Nordstedt, Arrest of β-Amyloid Fibril Formation by a Pentapeptide Ligand, *J. Biol. Chem.*, 1996, **271**(15), 8545–8548, DOI: 10.1074/jbc.271.15.8545.

16 H. Cheruvara, V. L. Allen-Baume, N. M. Kad and J. M. Mason, Intracellular Screening of a Peptide Library to Derive a Potent Peptide Inhibitor of α-Synuclein Aggregation, *J. Biol. Chem.*, 2015, **290**(12), 7426–7435, DOI: 10.1074/jbc.M114.620484.

17 W. Liu, F. Sun, M. Wan, F. Jiang, X. Bo, L. Lin, H. Tang and S. Xu, β-Sheet Breaker Peptide-HPYD for the Treatment of Alzheimer's Disease: Primary Studies on Behavioral Test and Transcriptional Profiling, *Front. Pharmacol.*, 2018, **8**, 1–13, DOI: 10.3389/fphar.2017.00969.

18 J. R. Horsley, B. Jovcevski, K. L. Wegener, J. Yu, T. L. Pukala and A. D. Abell, Rationally Designed Peptide-Based Inhibitor of Aβ42fibril Formation and Toxicity: A Potential Therapeutic Strategy for Alzheimer's Disease, *Biochem. J.*, 2020, **477**(11), 1541–1564, DOI: 10.1042/BCJ20200290.

19 B. Popova, D. Wang, A. Rajavel, K. Dhamotharan, D. F. Lázaro, J. Gerke, J. F. Uhrig, M. Hoppert, T. F. Outeiro and G. H. Braus, Identification of Two Novel Peptides That Inhibit α-Synuclein Toxicity and Aggregation, *Front. Mol. Neurosci.*, 2021, **14**, 1–18, DOI: 10.3389/fnmol.2021.659926.

20 M. Muttenthaler, G. F. King, D. J. Adams and P. F. Alewood, Trends in Peptide Drug Discovery, *Nat. Rev. Drug Discovery*, 2021, **20**(4), 309–325, DOI: 10.1038/s41573-020-00135-8.

21 L. Wang, N. Wang, W. Zhang, X. Cheng, Z. Yan, G. Shao, X. Wang, R. Wang and C. Fu, Therapeutic Peptides: Current Applications and Future Directions, *Signal Transduction Targeted Ther.*, 2022, **7**, 48, DOI: 10.1038/s41392-022-00904-4.

22 G. D. Maio, V. Monda, A. Messina, R. Polito, M. Monda, A. Asmundo, N. D. Nunno, I. Villano and V. C. Francavilla, Nanocarriers as a Possible Neuropeptides Delivery Systems in the Brain, *Acta Med. Mediterr.*, 2020, **36**(4), 2287–2292, DOI: 10.19193/0393-6384_2020_4_356.

23 M. W. Seo and T. E. Park, Recent Advances with Liposomes as Drug Carriers for Treatment of Neurodegenerative Diseases, *Biomed. Eng. Lett.*, 2021, **11**(3), 211–216, DOI: 10.1007/s13534-021-00198-5.

24 N. Rezaei, F. Mehrnejad, Z. Vaezi, M. Sedghi, S. M. Asghari and H. Naderi-Manesh, Encapsulation of an Endostatin Peptide in Liposomes: Stability, Release, and Cytotoxicity Study, *Colloids Surf., B*, 2020, **185**, 110552, DOI: 10.1016/j.colsurfb.2019.110552.

25 M. Sela, M. Poley, P. Mora-Raimundo, S. Kagan, A. Avital, M. Kaduri, G. Chen, O. Adir, A. Rozencweig, Y. Weiss, O. Sade, Y. Leichtmann-Bardoogo, L. Simchi, S. Aga-Mizrachi, B. Bell, Y. Yeretz-Peretz, A. Z. Or, A. Choudhary, I. Rosh, D. Cordeiro, S. Cohen-Adiv, Y. Berdichevsky, A. Odeh, J. Shklover, J. Shainsky-Roitman, J. E. Schroeder, D. Hershkovitz, P. Hasson, A. Ashkenazi, S. Stern, T. Laviv, A. Ben-Zvi, A. Avital, U. Ashery, B. M. Maoz and

A. Schroeder, Brain-Targeted Liposomes Loaded with Monoclonal Antibodies Reduce Alpha-Synuclein Aggregation and Improve Behavioral Symptoms in Parkinson's Disease, *Adv. Mater.*, 2023, **35**(51), 1–25, DOI: 10.1002/adma.202304654.

26 Q. Shan, Y. Zhi, Y. Chen, W. Yao, H. Zhou, J. Che and F. Bai, Intranasal Liposomes Co-Delivery of Aβ-Targeted KLVFF and ROS-Responsive Ceria for Synergistic Therapy of Alzheimer's Disease, *Chem. Eng. J.*, 2024, **494**, 153210, DOI: 10.1016/j.cej.2024.153210.

27 X. Zheng, X. Shao, C. Zhang, Y. Tan, Q. Liu, X. Wan, Q. Zhang, S. Xu and X. Jiang, Intranasal H102 Peptide-Loaded Liposomes for Brain Delivery to Treat Alzheimer's Disease, *Pharm. Res.*, 2015, **32**(12), 3837–3849, DOI: 10.1007/s11095-015-1744-9.

28 C. Hetényi, Z. Szabó, É. Klement, Z. Datki, T. Kórtvélyesi, M. Zarándi and B. Penke, Pentapeptide Amides Interfere with the Aggregation of β-Amyloid Peptide of Alzheimer's Disease, *Biochem. Biophys. Res. Commun.*, 2002, **292**(4), 931–936, DOI: 10.1006/bbrc.2002.6745.

29 M. H. Viet, S. T. Ngo, N. S. Lam and M. S. Li, Inhibition of Aggregation of Amyloid Peptides by Beta-Sheet Breaker Peptides and Their Binding Affinity, *J. Phys. Chem. B*, 2011, **115**(22), 7433–7446, DOI: 10.1021/jp1116728.

30 G. Gul, In Silico Screening of Peptide Inhibitors Targeting α-Synuclein for Parkinson's Disease, *J. Mol. Graphics Modell.*, 2025, **139**, 109079, DOI: 10.1016/j.jmgm.2025.109079.

31 K. Abe, N. Kobayashi, K. Sode and K. Ikebukuro, Peptide Ligand Screening of α-Synuclein Aggregation Modulators by in Silico Panning, *BMC Bioinformatics*, 2007, **8**, 1–7, DOI: 10.1186/1471-2105-8-451.

32 K. Kundal, S. Paramasivam, A. Mitra and N. Sarkar, Identification of Novel Peptides as Potential Modulators of Aβ42 Amyloidogenesis: An in Silico Approach, *Curr. Comput.-Aided Drug Des.*, 2023, **19**(4), 288–299, DOI: 10.2174/1573409919666230112170012.

33 N. Xiong, X. Y. Dong, J. Zheng, F. F. Liu and Y. Sun, Design of LVFFARK and LVFFARK-Functionalized Nanoparticles for Inhibiting Amyloid β-Protein Fibrillation and Cytotoxicity, *ACS Appl. Mater. Interfaces*, 2015, **7**(10), 5650–5662, DOI: 10.1021/acsami.5b00915.

34 S. R. Hughes, S. Goyal, J. E. Sun, P. Gonzalez-DeWhitt, M. Fortes, N. G. Riedel and S. R. Sahasrabudhe, Two-Hybrid System as a Model to Study the Interaction of β-Amyloid Peptide Monomers, *Proc. Natl. Acad. Sci. U. S. A.*, 1996, **93**(5), 2065–2070, DOI: 10.1073/pnas.93.5.2065.

35 J. F. Poduslo, G. L. Curran, A. Kumar, B. Frangione and C. Soto, β-Sheet Breaker Peptide Inhibitor of Alzheimer's Amyloidogenesis with Increased Blood-Brain Barrier Permeability and Resistance to Proteolytic Degradation in Plasma, *J. Neurobiol.*, 1999, **39**(3), 371–382, DOI: 10.1002/(SICI)1097-4695(19990605)39:3<371::AID-NEU4>3.0.CO;2-E.

36 R. J. Chalifour, R. W. McLaughlin, L. Lavoie, C. Morissette, N. Tremblay, M. Boulé, P. Sarazin, D. Stéa, D. Lacombe, P. Tremblay and F. Gervais, Stereoselective Interactions of Peptide Inhibitors with the β-Amyloid Peptide, *J. Biol. Chem.*, 2003, **278**(37), 34874–34881, DOI: 10.1074/jbc.M212694200.

37 O. M. A. El-Agnaf, K. E. Paleologou, B. Greer, A. M. Abogrein, J. E. King, S. A. Salem, N. J. Fullwood, F. E. Benson, R. Hewitt, K. J. Ford, F. L. Martin, P. Harriott, M. R. Cookson and D. Allsop, A Strategy for Designing Inhibitors of α –synuclein Aggregation and Toxicity as a Novel Treatment for Parkinson's Disease and Related Disorders, *FASEB J.*, 2004, **18**(11), 1315–1317, DOI: 10.1096/fj.03-1346fje.

38 Z. Datki, R. Papp, D. Zádori, K. Soós, L. Fülöp, A. Juhász, G. Laskay, C. Hetényi, E. Mihalik, M. Zarándi and B. Penke, In Vitro Model of Neurotoxicity of Aβ 1-42 and Neuroprotection by a Pentapeptide: Irreversible Events during the First Hour, *Neurobiol. Dis.*, 2004, **17**(3), 507–515, DOI: 10.1016/j.nbd.2004.08.007.

39 B. M. Austen, K. E. Paleologou, S. A. E. Ali, M. M. Qureshi, D. Allsop and O. M. A. El-Agnaf, Designing Peptide Inhibitors for Oligomerization and Toxicity of Alzheimer's β-Amyloid Peptide, *Biochemistry*, 2008, **47**(7), 1984–1992, DOI: 10.1021/bi701415b.

40 K. Wiesehan, J. Stöhr, L. Nagel-Steger, T. Van Groen, D. Riesner and D. Willbold, Inhibition of Cytotoxicity and Amyloid Fibril Formation by a D-Amino Acid Peptide That Specifically Binds to Alzheimer's Disease Amyloid Peptide, *Protein Eng., Des. Sel.*, 2008, **21**(4), 241–246, DOI: 10.1093/protein/gzm054.

41 T. Van Groen, K. Wiesehan, S. A. Funke, I. Kadish, L. Nagel-Steger and D. Willbold, Reduction of Alzheimer's Disease Amyloid Plaque Load in Transgenic Mice by D3, a D-Enantiomeric Peptide Identified by Mirror Image Phage Display, *ChemMedChem*, 2008, **3**(12), 1848–1852, DOI: 10.1002/cmdc.200800273.

42 Y. S. Kim, D. Lim, J. Y. Kim, S. J. Kang, Y. H. Kim and H. Im, β-Sheet-Breaking Peptides Inhibit the Fibrillation of Human α-Synuclein, *Biochem. Biophys. Res. Commun.*, 2009, **387**(4), 682–687, DOI: 10.1016/j.bbrc.2009.07.083.

43 R. Shaltiel-Karyo, M. Frenkel-Pinter, N. Egoz-Matia, A. Frydman-Marom, D. E. Shalev, D. Segal and E. Gazit, Inhibiting α-Synuclein Oligomerization by Stable Cell-Penetrating β-Synuclein Fragments Recovers Phenotype of Parkinson's Disease Model Flies, *PLoS One*, 2010, **5**(11), e13863, DOI: 10.1371/journal.pone.0013863.

44 S. Jagota and J. Rajadas, The Role of Pro, Gly Lys, and Arg Containing Peptides on Amyloid-Beta Aggregation, *Int. J. Pept. Res. Ther.*, 2012, **18**(1), 53–61, DOI: 10.1007/s10989-011-9278-4.

45 J. Liu, W. Wang, Q. Zhang, S. Zhang and Z. Yuan, Study on the Efficiency and Interaction Mechanism of a Decapeptide Inhibitor of β-Amyloid Aggregation, *Biomacromolecules*, 2014, **15**(3), 931–939, DOI: 10.1021/bm401795e.

46 V. Minicozzi, R. Chiaraluce, V. Consalvi, C. Giordano, C. Narcisi, P. Punzi, G. C. Rossi and S. Morante,

Computational and Experimental Studies on β-Sheet Breakers Targeting Aβ1-40 Fibrils, *J. Biol. Chem.*, 2014, **289**(16), 11242–11252, DOI: 10.1074/jbc.M113.537472.

47 L. X. Lin, X. Y. Bo, Y. Z. Tan, F. X. Sun, M. Song, J. Zhao, Z. H. Ma, M. Li, K. J. Zheng and S. M. Xu, Feasibility of β-Sheet Breaker Peptide-H102 Treatment for Alzheimer's Disease Based on β-Amyloid Hypothesis, *PLoS One*, 2014, **9**(11), 1–10, DOI: 10.1371/journal.pone.0112052.

48 S. Bansal, I. K. Maurya, N. Yadav, C. K. Thota, V. Kumar, K. Tikoo, V. S. Chauhan and R. Jain, C-Terminal Fragment, Aβ32-37, Analogues Protect Against Aβ Aggregation-Induced Toxicity, *ACS Chem. Neurosci.*, 2016, **7**(5), 615–623, DOI: 10.1021/acschemneuro.6b00006.

49 A. N. Klein, T. Ziehm, M. Tusche, J. Buitenhuis, D. Bartnik, A. Boeddrich, T. Wiglenda, E. Wanker, S. A. Funke, O. Brener, L. Gremer, J. Kutzsche and D. Willbold, Optimization of the All-D Peptide D3 for Aβ Oligomer Elimination, *PLoS One*, 2016, **11**(4), e0153035, DOI: 10.1371/journal.pone.0153035.

50 N. Rezaeian, N. Shirvanizadeh, S. Mohammadi, M. Nikkhah and S. S. Arab, The Inhibitory Effects of Biomimetically Designed Peptides on α-Synuclein Aggregation, *Arch. Biochem. Biophys.*, 2017, **634**, 96–106, DOI: 10.1016/j.abb.2017.09.015.

51 W. Liu, F. Sun, M. Wan, F. Jiang, X. Bo, L. Lin, H. Tang and S. Xu, β-Sheet Breaker Peptide-HPYD for the Treatment of Alzheimer's Disease: Primary Studies on Behavioral Test and Transcriptional Profiling, *Front. Pharmacol.*, 2018, **8**, 1–13, DOI: 10.3389/fphar.2017.00969.

52 R. M. Meade, K. J. C. Watt, R. J. Williams and J. M. Mason, A Downsized and Optimised Intracellular Library-Derived Peptide Prevents Alpha-Synuclein Primary Nucleation and Toxicity Without Impacting Upon Lipid Binding, *J. Mol. Biol.*, 2021, **433**(24), 167323, DOI: 10.1016/j.jmb.2021.167323.

53 S. Nim, D. M. O. Hara, C. Corbi-verge, A. Perez-riba, K. Fujisawa, M. Kapadia, H. Chau, F. Albanese, G. Pawar, M. L. D. Snoo, S. G. Ngana, J. Kim, O. M. A. El-agnaf, E. Rennella and L. E. Kay, Disrupting the α-Synuclein-ESCRT Interaction with a Peptide Inhibitor Mitigates Neurodegeneration in Preclinical Models of Parkinson's Disease, *Nat. Commun.*, 2023, **14**, 2150, DOI: 10.1038/s41467-023-37464-2.

54 M. Z. Tien, D. K. Sydykova, A. G. Meyer and C. O. Wilke, Peptidebuilder: A Simple Python Library to Generate Model Peptides, *PeerJ*, 2013, **2013**(1), 1–10, DOI: 10.7717/peerj.80.

55 M. H. M. Olsson, C. R. Søndergaard, M. Rostkowski and J. H. Jensen, PROPKA3: Consistent Treatment of Internal and Surface Residues in Empirical p K a Predictions, *J. Chem. Theory Comput.*, 2011, **7**(2), 525–537, DOI: 10.1021/ct100578z.

56 *Schrödinger Release 2025-4: SiteMap*, Schrödinger, LLC, New York, NY, 2025.

57 C. J. Hsieh, J. J. Ferrie, K. Xu, I. Lee, T. J. A. Graham, Z. Tu, J. Yu, D. Dhavale, P. Kotzbauer, E. J. Petersson and R. H. Mach, A-synuclein Fibrils Contain Multiple Binding Sites for Small Molecules, *ACS Chem. Neurosci.*, 2018, **9**(11), 2521–2527, DOI: 10.1021/acschemneuro.8b00177.

58 A. Cornejo, J. Caballero, M. Simirgiotis, V. Torres, L. Sánchez, N. Díaz, M. Guimaraes, M. Hernández, C. Areche, S. Alfaro, L. Caballero and F. Melo, Dammarane Triterpenes Targeting α-Synuclein: Biological Activity and Evaluation of Binding Sites by Molecular Docking, *J. Enzyme Inhib. Med. Chem.*, 2021, **36**(1), 154–162, DOI: 10.1080/14756366.2020.1851216.

59 E. F. Marondedze, K. K. Govender and P. P. Govender, Computational Investigation of the Binding Characteristics of β-Amyloid Fibrils, *Biophys. Chem.*, 2020, **256**, 106281, DOI: 10.1016/j.bpc.2019.106281.

60 Y. Zhang and M. F. Sanner, AutoDock CrankPep: Combining Folding and Docking to Predict Protein-Peptide Complexes, *Bioinformatics*, 2019, **35**(24), 5121–5127, DOI: 10.1093/bioinformatics/btz459.

61 P. Zhou, B. Jin, H. Li and S. Y. Huang, HPEPDOCK: A Web Server for Blind Peptide-Protein Docking Based on a Hierarchical Algorithm, *Nucleic Acids Res.*, 2018, **46**(W1), W443–W450, DOI: 10.1093/nar/gky357.

62 S. Jo, T. Kim, V. G. Iyer and W. Im, CHARMM-GUI: A Web-based Graphical User Interface for CHARMM, *J. Comput. Chem.*, 2008, **29**, 1859–1865, DOI: 10.1002/jcc.20945.

63 S. Park, Y. K. Choi, S. Kim, J. Lee and W. Im, CHARMM-GUI Membrane Builder for Lipid Nanoparticles with Ionizable Cationic Lipids and PEGylated Lipids, *J. Chem. Inf. Model.*, 2021, **61**(10), 5192–5202, DOI: 10.1021/acs.jcim.1c00770.

64 E. Lindahl, M. Abraham, B. Hess and D. van der Spoel, *GROMACS 2021.3 Source code, (2021.3)*.

65 J. Huang, S. Rauscher, G. Nawrocki, T. Ran, M. Feig, B. L. d. Groot, H. Grubmüller and A. D. MacKerell Jr., CHARMM36m: An Improved Force Field for Folded and Intrinsically Disordered Proteins, *Nat. Methods*, 2017, **14**(1), 71–73, DOI: 10.1038/nmeth.4067.

66 T. Darden, D. York and L. Pedersen, Particle Mesh Ewald: An N·log(N) Method for Ewald Sums in Large Systems, *J. Chem. Phys.*, 1993, **98**(12), 10089–10092, DOI: 10.1063/1.464397.

67 B. Hess, H. Bekker, H. J. C. Berendsen and J. G. E. M. Fraaije, LINCS: A Linear Constraint Solver for Molecular Simulations, *J. Comput. Chem.*, 1997, **18**(12), 1463–1472, DOI: 10.1002/(SICI)1096-987X(199709)18:12<1463::AID-JCC4>3.0.CO;2-H.

68 G. Bussi, D. Donadio and M. Parrinello, Canonical Sampling through Velocity Rescaling, *J. Chem. Phys.*, 2007, **126**, 014101, DOI: 10.1063/1.2408420.

69 M. Parrinello and A. Rahman, Polymorphic Transitions in Single Crystals: A New Molecular Dynamics Method, *J. Appl. Phys.*, 1981, **52**(12), 7182–7190, DOI: 10.1063/1.328693.

70 M. S. Valdés-Tresanco, M. E. Valdés-Tresanco, P. A. Valiente and E. Moreno, Gmx_MMPBSA: A New Tool to Perform End-State Free Energy Calculations with

GROMACS, *J. Chem. Theory Comput.*, 2021, **17**(10), 6281–6291, DOI: 10.1021/acs.jctc.1c00645.

71 W. Humphrey, A. Dalke and K. Schulten, VMD: Visual Molecular Dynamics, *J. Mol. Graphics*, 1996, **14**, 33–38.

72 A. C. Wallace, R. A. Laskowski and J. M. Thornton, Ligplot: A Program to Generate Schematic Diagrams of Protein-Ligand Interactions, *Protein Eng., Des. Sel.*, 1995, **8**(2), 127–134, DOI: 10.1093/protein/8.2.127.

73 T. Róg, M. Pasenkiewicz-Gierula, I. Vattulainen and M. Karttunen, Ordering Effects of Cholesterol and Its Analogues, *Biochim. Biophys. Acta, Biomembr.*, 2009, **1788**(1), 97–121, DOI: 10.1016/j.bbamem.2008.08.022.

74 A. Magarkar, T. Róg and A. Bunker, Molecular Dynamics Simulation of PEGylated Membranes with Cholesterol: Building toward the DOXIL Formulation, *J. Phys. Chem. C*, 2014, **118**(28), 15541–15549, DOI: 10.1021/jp504962m.

75 T. J. Piggot, J. R. Allison, R. B. Sessions and J. W. Essex, On the Calculation of Acyl Chain Order Parameters from Lipid Simulations, *J. Chem. Theory Comput.*, 2017, **13**(11), 5683–5696, DOI: 10.1021/acs.jctc.7b00643.

76 P. C. T. Souza, R. Alessandri, J. Barnoud, S. Thallmair, I. Faustino, F. Grünewald, I. Patmanidis, H. Abdizadeh, B. M. H. Bruininks, T. A. Wassenaar, P. C. Kroon, J. Melcr, V. Nieto, V. Corradi, H. M. Khan, J. Domański, M. Javanainen, H. Martinez-Seara, N. Reuter, R. B. Best, I. Vattulainen, L. Monticelli, X. Periole, D. P. Tieleman, A. H. de Vries and S. J. Marrink, Martini 3: A General Purpose Force Field for Coarse-Grained Molecular Dynamics, *Nat. Methods*, 2021, **18**(4), 382–388, DOI: 10.1038/s41592-021-01098-3.

77 F. Grünewald, R. Alessandri, P. C. Kroon, L. Monticelli, P. C. T. Souza and S. J. Marrink, Polyply; a Python Suite for Facilitating Simulations of Macromolecules and Nanomaterials, *Nat. Commun.*, 2022, **13**(1), 1–12, DOI: 10.1038/s41467-021-27627-4.

78 H. J. C. Berendsen, J. P. M. Postma, W. F. Van Gunsteren, A. Dinola and J. R. Haak, Molecular Dynamics with Coupling to an External Bath, *J. Chem. Phys.*, 1984, **81**(8), 3684–3690, DOI: 10.1063/1.448118.

79 I. G. Tironi, R. Sperb, P. E. Smith and W. F. van Gunsteren, A Generalized Reaction Field Method for Molecular Dynamics Simulations, *J. Chem. Phys.*, 1995, **102**, 5451–5459.

80 G. Kogkos, F. Gkartziou, S. Mourtas, K. K. Barlos, P. Klepetsanis, K. Barlos and S. G. Antimisiaris, Liposomal Entrapment or Chemical Modification of Relaxin2 for Prolongation of Its Stability and Biological Activity, *Biomolecules*, 2022, **12**(10), 1362, DOI: 10.3390/biom12101362.

81 A. Vitali, P. Paolicelli, B. Bigi, J. Trilli, L. Di Muzio, V. C. Carriero, M. A. Casadei and S. Petralito, Liposome Encapsulation of the Palmitoyl–KTTKS Peptide: Structural and Functional Characterization, *Pharmaceutics*, 2024, **16**(2), 219, DOI: 10.3390/pharmaceutics16020219.

82 H. Okumura and S. G. Itoh, Molecular Dynamics Simulation Studies on the Aggregation of Amyloid-β Peptides and Their Disaggregation by Ultrasonic Wave and Infrared Laser Irradiation, *Molecules*, 2022, **27**(8), 2483, DOI: 10.3390/molecules27082483.

83 J. Chen, N. Sawyer and L. Regan, Protein-Protein Interactions: General Trends in the Relationship between Binding Affinity and Interfacial Buried Surface Area, *Protein Sci.*, 2013, **22**(4), 510–515, DOI: 10.1002/pro.2230.

84 A. A. Radwan, F. K. Alanazi and M. Raish, Design and Synthesis of Multi-Functional Small-Molecule Based Inhibitors of Amyloid-β Aggregation: Molecular Modeling and in Vitro Evaluation, *PLoS One*, 2023, **18**, 1–20, DOI: 10.1371/journal.pone.0286195.

85 J. M. Jakubowski, A. A. Orr, D. A. Le and P. Tamamis, Interactions between Curcumin Derivatives and Amyloid-β Fibrils: Insights from Molecular Dynamics Simulations, *J. Chem. Inf. Model.*, 2020, **60**(1), 289–305, DOI: 10.1021/acs.jcim.9b00561.

86 F. A. Buratti, N. Boeffinger, H. A. Garro, J. S. Flores, F. J. Hita, P. d. C. Gonçalves, F. d. R. Copello, L. Lizarraga, G. Rossetti, P. Carloni, M. Zweckstetter, T. F. Outeiro, S. Eimer, C. Griesinger and C. O. Fernández, Aromaticity at Position 39 in α-Synuclein: A Modulator of Amyloid Fibril Assembly and Membrane-Bound Conformations, *Protein Sci.*, 2022, **31**(7), 1–12, DOI: 10.1002/pro.4360.

87 J. Y. O'Shea, D. D. Dhavale, H. Hwang, Z. Smith, T. J. A. Graham, R. H. Mach and P. T. Kotzbauer, Use of Amplified Lewy Body Dementia Fibrils and Autoradiography to Characterize Binding of Radioligand Tg-1-90B to Alpha-Synuclein Fibrils in Postmortem Brain Tissue, *Cells*, 2025, **14**(18), 4–6, DOI: 10.3390/cells14181477.

88 S. Capponi, J. A. Freites, D. J. Tobias and S. H. White, Interleaflet Mixing and Coupling in Liquid-Disordered Phospholipid Bilayers, *Biochim. Biophys. Acta, Biomembr.*, 2016, **1858**(2), 354–362, DOI: 10.1016/j.bbamem.2015.11.024.

89 B. N. Olsen, A. A. Bielska, T. Lee, M. D. Daily, D. F. Covey, P. H. Schlesinger, N. A. Baker and D. S. Ory, The Structural Basis of Cholesterol Accessibility in Membranes, *Biophys. J.*, 2013, **105**(8), 1838–1847, DOI: 10.1016/j.bpj.2013.08.042.

90 G. Gul, R. Faller and N. Ileri-Ercan, Polystyrene-Modified Carbon Nanotubes: Promising Carriers in Targeted Drug Delivery, *Biophys. J.*, 2022, **121**(22), 4271–4279, DOI: 10.1016/j.bpj.2022.10.014.

91 G. Gul, R. Faller and N. Ileri-ercan, Coarse-Grained Modeling of Polystyrene-Modified CNTs and Their Interactions with Lipid Bilayers, *Biophys. J.*, 2023, **122**, 1–14, DOI: 10.1016/j.bpj.2023.04.005.

92 A. Filippov, G. Orädd and G. Lindblom, The Effect of Cholesterol on the Lateral Diffusion of Phospholipids in Oriented Bilayers, *Biophys. J.*, 2003, **84**(5), 3079–3086, DOI: 10.1016/S0006-3495(03)70033-2.

93 H. Nanda, V. García Sakai, S. Khodadadi, M. Tyagi, E. J. Schwalbach and J. E. Curtis, Relaxation Dynamics of Saturated and Unsaturated Oriented Lipid Bilayers, *Soft*

Matter, 2018, **14**(29), 6119–6127, DOI: 10.1039/c7sm01720k.

94 S. Singh, P. Papareddy, M. Mörgelin, A. Schmidtchen and M. Malmsten, Effects of PEGylation on Membrane and Lipopolysaccharide Interactions of Host Defense Peptides, *Biomacromolecules*, 2014, **15**(4), 1337–1345, DOI: 10.1021/bm401884e.

95 J. E. Nielsen, N. König, S. Yang, M. W. A. Skoda, A. Maestro, H. Dong, M. Cárdenas and R. Lund, Lipid Membrane Interactions of Self-Assembling Antimicrobial Nanofibers: Effect of PEGylation, *RSC Adv.*, 2020, **10**(58), 35329–35340, DOI: 10.1039/d0ra07679a.

96 Z. Deng, X. Lu, C. Xu, B. Yuan and K. Yang, Lipid-Specific Interactions Determine the Organization and Dynamics of Membrane-Active Peptide Melittin, *Soft Matter*, 2020, **16**(14), 3498–3504, DOI: 10.1039/d0sm00046a.

97 N. Schmidt, A. Mishra, G. H. Lai and G. C. L. Wong, Arginine-Rich Cell-Penetrating Peptides, *FEBS Lett.*, 2010, **584**(9), 1806–1813, DOI: 10.1016/j.febslet.2009.11.046.

98 A. Mohan, S. R. C. K. Rajendran, J. Thibodeau, L. Bazinet and C. C. Udenigwe, Liposome Encapsulation of Anionic and Cationic Whey Peptides: Influence of Peptide Net Charge on Properties of the Nanovesicles, *LWT–Food Sci. Technol.*, 2018, **87**, 40–46, DOI: 10.1016/j.lwt.2017.08.072.

99 H. I. Ingólfsson, C. A. Lopez, J. J. Uusitalo, D. H. de Jong, S. M. Gopal, X. Periole and S. J. Marrink, The Power of Coarse Graining in Biomolecular Simulations, *Wiley Interdiscip. Rev.: Comput. Mol. Sci.*, 2014, **4**(3), 225–248, DOI: 10.1002/wcms.1169.

100 F. T. Doole, T. Kumarage, R. Ashkar and M. F. Brown, Cholesterol Stiffening of Lipid Membranes, *J. Membr. Biol.*, 2022, **255**(4–5), 385–405, DOI: 10.1007/s00232-022-00263-9.

101 Z. Chen and R. P. Rand, The Influence of Cholesterol on Phospholipid Membrane Curvature and Bending Elasticity, *Biophys. J.*, 1997, **73**(1), 267–276, DOI: 10.1016/S0006-3495(97)78067-6.

102 J. Gubernator, Active Methods of Drug Loading into Liposomes: Recent Strategies for Stable Drug Entrapment and Increased in Vivo Activity, *Expert Opin. Drug Delivery*, 2011, **8**(5), 565–580, DOI: 10.1517/17425247.2011.566552.